Monthly Notices
of the
ROYAL ASTRONOMICAL SOCIETY

MNRAS **488,** 4504–4519 (2019)
Advance Access publication 2019 July 25

doi:10.1093/mnras/stz2039

Scaling relations for globular cluster systems in early-type galaxies

Juan P. Caso,[1,2]★ Bruno J. De Bórtoli,[1,2] Ana I. Ennis[1,2] and Lilia P. Bassino[1,2]

[1]*Facultad de Ciencias Astronómicas y Geofísicas de la Universidad Nacional de La Plata, and Instituto de Astrofísica de La Plata (CCT La Plata – CONICET, UNLP), Paseo del Bosque S/N, B1900FWA La Plata, Argentina*
[2]*Consejo Nacional de Investigaciones Científicas y Técnicas, Godoy Cruz 2290, C1425FQB Ciudad Autónoma de Buenos Aires, Argentina*

Accepted 2019 July 23. Received 2019 July 22; in original form 2019 April 12

ABSTRACT

The formation and growth of globular cluster systems (GCSs) is closely related to the evolutionary processes experienced by their host galaxies. In particular, their radial distributions scale with several properties of the galaxies and their haloes. We performed a photometric study, by means of HST/ACS archival data of several intermediate luminosity galaxies located in low-density environments. It was supplemented with available photometric data of GCSs from the Virgo and Fornax clusters, resulting in a sample of almost 30 GCSs for which we fitted their radial profiles. The resulting overall properties agree with those from previous studies, as we found that the effective radius, extension, and concentration of the GCS radial profiles correlate with the stellar mass, effective radius, and number of globular clusters, presenting in some cases a bilinear relation. The extension also correlates with the central velocity dispersion for central galaxies, but not for satellites. From a statistical comparison with numerical simulations we obtained good agreement between the effective radius and extension of the GCS scale with the effective and virial radius of the haloes, respectively. Finally, we analysed these results in the literature context.

Key words: galaxies: elliptical and lenticular, cD – galaxies: evolution – galaxies: haloes – galaxies: star clusters: general.

1 INTRODUCTION

Radial profiles of globular cluster systems (GCSs) have been extensively analysed in literature as part of the general context of the globular clusters (GCs) in individual galaxies (e.g. Usher et al. 2013; Durrell et al. 2014; Caso et al. 2019). GCSs span a broad range of properties, with giant ellipticals usually presenting several thousand members and large systems up to several tens of kiloparsecs from the galaxy centre (e.g. Dirsch et al. 2003; Bassino et al. 2006a). On the other hand, dwarf galaxies usually have a few members (e.g. Peng et al. 2008; Georgiev et al. 2009).

The connection of the GCS with both the stellar and halo (i.e. stellar plus dark) mass distributions of the host galaxy is well known, with metal-rich GCs tracing the surface-brightness profile of the host galaxy and metal-poor ones presenting a more extended distribution (Bassino, Richtler & Dirsch 2008; Foster et al. 2011; Bassino & Caso 2017), similar to the X-ray emission of the hot gas (Forbes, Ponman & O'Sullivan 2012; Escudero et al. 2015). These properties of GCSs in luminous early-type galaxies have been interpreted as evidence of the presence of two GC sub-populations with different origins. In the current paradigm where GCs were formed during major starburst episodes (Kruijssen 2014), the origin of metal-poor GCs is connected with the primordial building blocks of the galaxies, while metal-rich ones have their origin in later major mergers (Muratov & Gnedin 2010; Li & Gnedin 2014; Choksi, Gnedin & Li 2018). The accretion of satellite galaxies was also relevant in the build-up of the metal-poor population (Tonini 2013). Observations support this scenario of two phases, with the mean colours of the GCs presenting a colour gradient, getting more metal-poor towards larger galactocentric distances (Forbes et al. 2011; Caso, Bassino & Gómez 2017; Forbes & Remus 2018). In this sense, Peng et al. (2006) found that the colour range spanned by a GCS correlates with the galaxy stellar mass, in a way that the bluer colours present in the outer part of GCSs agree with the main role assumed by accretion.

Some galaxies that have suffered late mergers present evidence of the existence of intermediate age GCs (Strader, Brodie & Forbes 2004; Caso, Bassino & Gómez 2015; Sesto, Faifer & Forte 2016), deviating from the typical scenario of two sub-populations.

The size–mass relation for galaxies is well documented in the literature (Spindler & Wake 2017, and references therein), so that it is natural to wonder whether a similar relation exists for GCSs. A first attempt was made by Rhode et al. (2007), comparing the extent of the GCS with the stellar mass of their host galaxy for a small sample. Kartha et al. (2014) analysed the behaviour of the effective radius of the GCS with the stellar mass and the effective radius of the galaxy. More recently, Forbes (2017) compared the extension

★ E-mail: jpcaso@fcaglp.unlp.edu.ar

of the GCS in early-type galaxies with the host galaxy size and its virial radius. In these studies a correlation seems to exist between the parameters of the GCS and the host galaxy.

GCs have also proven to be useful tracers of the galaxy dynamics (Richtler 2013; Richtler et al. 2015; Alabi et al. 2017; Wasserman et al. 2018) up to large galactocentric distances (Schuberth et al. 2010, 2012), implying their dynamics is ruled by the total mass distribution. Spitler et al. (2008) redefined the T-parameter from Zepf & Ashman (1993), considering the halo mass instead of just the stellar mass, and suggested that GCs were formed in direct proportion to the halo mass of the host galaxy. Spitler & Forbes (2009) found that the total mass of the GCS scales with the halo mass, later confirmed by Hudson, Harris & Harris (2014). All these results point to a connection between the properties of the GCS and the mass distribution of the host galaxy, which has already been addressed by Hudson & Robison (2018) and Forbes et al. (2018) with samples of different characteristics.

We aim to extend the study of the scaling relations for GCSs to less massive early-type galaxies, taking advantage of a galaxy sample observed with the same instrument and similar photometric depth. In this context, we analyse relations found in literature for massive galaxies, looking for any possible changes when we move to less massive ones and poorer GCSs.

The paper is organized as follows. The observations and reduction procedures are described in Section 2, and the observational and numerical catalogues are indicated in Section 3. In Section 4 we present the results, and Section 5 is devoted to the discussion. Finally, in Section 6 we make a brief summary of the results.

2 OBSERVATIONAL DATA AND REDUCTION

The observational dataset consists of observations centred on nearby early-type galaxies, taken from the Mikulski Archive for Space Telescopes (MAST).[1] All the observations had been carried out with the HST/ACS Wide Field Camera (WFC), with filters commonly used in GCs studies. The analysed galaxies are listed in Table 1, in descending order of *B*-band luminosity, together with a log of the observations.

2.1 Photometry and source selection

The surface-brightness profile of each galaxy was obtained in both filters (see Table 1), using the task ELLIPSE within IRAF. The ellipse parameters, e.g. ellipticity, centre coordinates, and position angle, were fitted for the inner region of the galaxies, depending on the FOV and the galaxy surface brightness, typically up to ≈30 arcsec. For larger galactocentric distances these parameters were fixed.

Then, a synthetic model of the galaxies was generated and subtracted from the original image, to facilitate the detection of GC candidates. A first catalogue of sources was made with SExtractor (Bertin & Arnouts 1996), considering every detection of at least three connected pixels above a threshold of 3σ from the sky level as a positive identification. As shown in the literature, GC-like objects at distances similar to the ones corresponding to the galaxies in our sample might be marginally resolved (e.g. Jordán et al. 2004; Caso et al. 2014; Bassino & Caso 2017), and they usually present low eccentricities (e.g. Harris 2009a; Chiboucas et al. 2011). Then, in order to discard extended sources we selected those with elongation smaller than 2 and full width at half-maximum (FWHM) smaller than 5 px. Similar criteria have been previously used for identifying GCs on ACS images (e.g. Jordán et al. 2004, 2007).

Aperture photometry was performed in both filters with an aperture radius of 5 px. In order to calculate aperture corrections, we analysed the change in the correction value with the effective radius of the sources ($r_{\rm eff}$). As a first step, we carried out PSF photometry on images of 47 Tuc observed in dates close to the ones from the observations in our sample, and with the same filters. In each case, approximately 40–50 relatively isolated bright stars from the 47 Tuc images were used to obtain the PSF. The derived PSF typically had FWHM ≈0.08 arcsec. Then, the software ISHAPE (Larsen 1999) was used to calculate structural parameters for the sources in our photometric catalogue. We assumed a King profile (King 1962, 1966) with a concentration parameter, i.e. the ratio of tidal over core radius, $c = 30$, used in previous studies of GCs. The mode of the distribution of $r_{\rm eff}$ for the galaxies in our sample spans 0.015–0.035 arcsec, with a tail towards more extended objects.

Those objects with signal-to-noise ratio larger than 50 (a condition required for an accurate calculus of the structural parameters, according to Larsen 1999) were split in samples according to their $r_{\rm eff}$, and aperture corrections were calculated from each of them. This procedure allowed us to determine the variation in aperture correction with $r_{\rm eff}$, which was typically ≈0.06 mag for objects in the range 0.01 arcsec $< r_{\rm eff} <$ 0.08 arcsec, which represents more than 80 per cent of the GC candidates. Despite these variations, we applied mean corrections to GC candidates. These were calculated for candidates with $r_{\rm eff}$ around the mode of the distribution. Although the changes in the aperture corrections as a function of $r_{\rm eff}$ might be large, the present study is focused on analysing the radial distribution of GCs, and our simplified treatment does not lead to significant uncertainties in our results.

Table 1. Basic data from observations. The extinction values are those from the recalibration by Schlafly & Finkbeiner (2011).

Name	Filter	Obs. date (dd mm yyyy)	Exp. time (s)	Prog. ID	A_λ
NGC 3818	*F475W*	01 01 2006	1380	10554	0.12
	F850LP	01 01 2006	2987	10554	0.05
NGC 1340	*F475W*	20 09 2004	760	10217	0.06
	F850LP	20 09 2004	1130	10217	0.02
NGC 4621	*F475W*	19 07 2003	750	9401	0.11
	F850LP	19 07 2003	1120	9401	0.04
NGC 7173	*F475W*	16 05 2006	1375	10554	0.09
	F850LP	16 05 2006	3075	10554	0.03
NGC 1439	*F475W*	21 08 2006	1375	10554	0.10
	F850LP	21 08 2006	3023	10554	0.04
NGC 1426	*F475W*	21 08 2006	1375	10554	0.05
	F850LP	21 08 2006	3023	10554	0.02
NGC 3377	*F475W*	13 01 2006	1380	10554	0.11
	F850LP	13 01 2006	3005	10554	0.04
NGC 4033	*F475W*	04 01 2006	1380	10554	0.16
	F850LP	04 01 2006	3017	10554	0.06
NGC 1172	*F475W*	17 08 2006	1380	10554	0.22
	F850LP	17 08 2006	3005	10554	0.09

[1] Based on observations made with the NASA/ESA Hubble Space Telescope, obtained from the data archive at the Space Telescope Science Institute. STScI is operated by the Association of Universities for Research in Astronomy, Inc. under NASA contract NAS 5-26555.

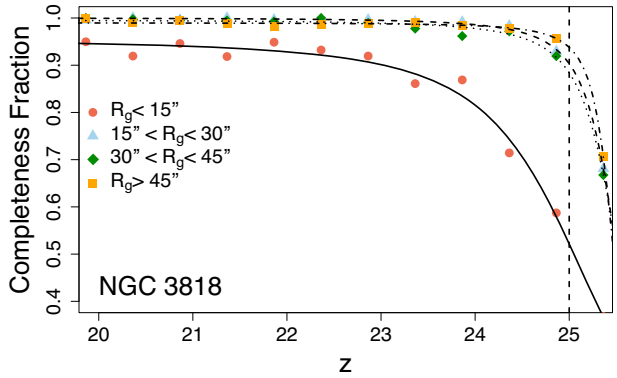

Figure 1. Completeness as a function of z magnitude for NGC 3818, obtained from 60 000 artificial stars. The completeness curves were calculated in for different galactocentric ranges (R_g), and the fits correspond to equation (2). The dashed vertical line at $z = 25$ mag indicates the assumed magnitude limit. Analogue analysis was performed for the other ellipticals in low-density environments.

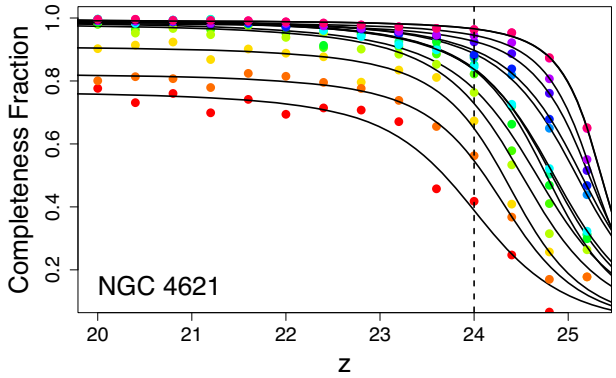

Figure 2. Completeness as a function of z magnitude for NGC 4621. A detailed analysis of the completeness behaviour at different radii was carried out from 250 000 artificial stars, in order to model the completeness for the rest of the galaxies in the Virgo cluster. Different colours identify completeness curves for different galactocentric radii, i.e. different surface-brightness levels, ranging from 17.4 to 21.9 mag arcsec^{-2} in the z filter. The dashed vertical line at $z = 24$ mag indicates a typical completeness limit.

2.2 Photometric calibration and extinction corrections

The instrumental magnitudes ($F475$, $F850$) were calibrated using the relation:

$$m_{\rm std} = m_{\rm inst} + {\rm ZP} \quad (1)$$

with $m_{\rm std}$ and $m_{\rm inst}$ the standard and instrumental magnitudes, respectively. The zero-points were taken from Sirianni et al. (2005), ZP$_{F475} = 26.068$ and ZP$_{F850} = 24.862$, and the resulting magnitudes correspond to g and z bands, respectively.

Then, we applied corrections due to Galactic extinction from Schlafly & Finkbeiner (2011), listed in the last column of Table 1.

Finally, we selected as GC candidates those sources with colours in the range $0.6 < (g - z)_0 < 1.7$, in agreement with previous studies in the same bands (e.g. Jordán et al. 2005; Cho et al. 2012).

2.3 Completeness analysis

The photometric completeness for each galaxy was obtained by adding artificial stars to the images in both bands. We added 50 artificial stars per image using the PSF previously obtained from the 47 Tuc exposures. These artificial sources span the colour range of GCs and $21 < z_0 < 26$. We repeated the process 1200 times to achieve a final sample of 60 000 artificial stars. The photometry was developed in the same manner as for the science fields, and the resulting catalogues were used to calculate the completeness curves in four different galactocentric ranges (Fig. 1). Typical completeness limits are selected at the z magnitude for which completeness levels fall below 90 per cent. In order to apply completeness corrections in our analysis, we fitted an analytic function of the form:

$$f(m) = \beta \left(1 - \frac{\alpha(m - m_0)}{\sqrt{1 + \alpha^2 (m - m_0)^2}}\right) \quad (2)$$

similar to that used by Harris et al. (2009), with β, α, and m_0 free parameters (curves are shown in Fig. 1).

The exception to this procedure were NGC 4621 and NGC 1340. In these cases a total of 250 000 artificial stars were added to the images in both bands, in order to obtain a more detailed evolution of the completeness curves as a function of the galactocentric radii (i.e. the surface-brightness level, see Fig. 2). From these we calculated the completeness corrections to be applied to the rest of the galaxies in their respective photometries.

3 DATA SOURCES FROM LITERATURE

3.1 Catalogues of GCs from Virgo and Fornax galaxies

We also fitted GCs radial profiles for a sample of ellipticals from the Virgo and Fornax clusters. We selected those galaxies which presented an intermediate luminosity, and a number of GCs large enough to allow their radial profile fitting. We used the available photometry from Jordán et al. (2009) and Jordán et al. (2015). In order to calculate the background level we used point sources in the ACS fields of several dwarf ellipticals, which present few GCs (Peng et al. 2008 for Virgo galaxies and Villegas et al. 2010 for Fornax ones). In order to apply completeness corrections to these photometries, we calculated the mean surface-brightness in the z band ($\mu_{{\rm mean},z}$) for different radial ranges, taking into account the profiles derived by Ferrarese et al. (2006) for galaxies in the Virgo cluster and profiles fitted by us for those belonging to Fornax. Then, we calculated the corresponding completeness corrections from the completeness curve that matches the $\mu_{{\rm mean},z}$ from the analysis described in the previous section for NGC 4621 and NGC 1340.

3.2 Dark matter simulation

We analysed the SMDPL cosmological dark matter simulation, which is part of the Multidark project (Klypin et al. 2016), and is publicly available through the official database of the project.[2] This simulation consists of a periodic cubic volume of $400\,h^{-1}$Mpc of size length, filled with 3840^3 particles with a mass of $9.63 \times 10^7\,h^{-1}{\rm M}_\odot$ and it considers the cosmological parameters of the Planck Collaboration XVI (2014). The dark matter haloes of the simulation detected with ROCKSTAR halo finder were analysed, specifically the catalogue corresponding to the local Universe ($z = 0$).

This catalogue includes the main host haloes found over the background density and the satellite haloes (or subhaloes) lying

[2] https://www.cosmosim.org/

within another halo. We consider each of these structures as the host of a unique galaxy, so the main ones correspond to the central galaxies of each system, and the satellite haloes, to the satellite galaxies. For each halo we extracted from the catalogue its position, mass, host/satellite relationships and the parameters of the mass profile.

In addition to the properties obtained from the catalogue, we assigned to each halo a luminosity in the K band by using a simple implementation of a halo occupation distribution (HOD; Conroy, Wechsler & Kravtsov 2006; Vale & Ostriker 2006) method, which appoints each luminosity in a non-parametric way. We assume a monotonic relation of the form

$$n_{\rm g}(>L) = n_{\rm h}(>M), \tag{3}$$

where $n_{\rm g}$ and $n_{\rm h}$ are the number density of galaxies and haloes, respectively. No distinction between main host and satellites was made. The number density of galaxies must preserve the parametric luminosity function (LF) derived by Schechter (1976), with the parameters for the K band measured by Kochanek et al. (2001) from the 2MASS survey. Expressing the Schechter LF in terms of the magnitude and starting from the bright end of the distribution, rest frame M_K magnitudes were assigned to all the haloes using a precision of 0.01 mag. The most massive main haloes in SMDPL present virial masses of $\approx 10^{15}$ M$_\odot$, which are similar to the typical total mass derived for the Coma cluster (e.g. Geller, Diaferio & Kurtz 1999; Łokas & Mamon 2003; Kubo et al. 2007). Hence, we assumed it as an observational analogue to these massive main haloes. Because of this we chose the luminosity of NGC 4889, its central galaxy, as the typical luminosity of a central galaxy belonging to these massive main haloes. Considering for NGC 4889 an apparent magnitude of $K = 8.4$ mag (Gavazzi & Boselli 1996) and a distance of 94 Mpc, obtained from NED,[3] its absolute magnitude in the K filter is $M_K = -26.5$. This value was used as the upper limit luminosity for the HOD method.

4 RESULTS

4.1 Galaxy surface-brightness profiles

Because a comprehensive analysis has been carried out for Virgo and Fornax galaxies by Ferrarese et al. (2006), Côté et al. (2007), and Glass et al. (2011), we focused on those located in low-density environments (HST programme ID 10554). The upper panels for each galaxy in Fig. 3 show the surface-brightness profiles in g (green circles) and z (red squares) bands as a function of the equivalent radius $r_{\rm eq}$. For each band we fitted Sérsic profiles (Sersic 1968) of the form:

$$\mu(r_{\rm eq}) = \mu_{\rm eff} + 1.0857 b_n \left[\left(\frac{r_{\rm eq}}{r_{\rm eff,gal}} \right)^{\frac{1}{n}} - 1 \right], \tag{4}$$

where $r_{\rm eq}$ and $r_{\rm eff,\,gal}$ are in arcsec, the latter one corresponding to the effective radius, $\mu(r_{\rm eq})$ and $\mu_{\rm eff}$ are in units of mag arcsec^{-2}, n is the Sérsic shape index, and b_n is calculated using the expression from Ciotti (1991). We considered a single component for the profiles corresponding to the field of view (FOV) of the ACS camera, achieving acceptable fits in all cases (see residuals in the middle panels in Fig. 3). Due to the reduced FOV, an accurate measurement of the background level was not possible. Hence, it was handled as a free parameter and it was fitted from the counts level for galactocentric distances larger than 100 arcsec. This value and the Sérsic profile were fitted iteratively, subtracting their corresponding contributions in each step. The procedure was repeated until the parameters converged and the residuals for the measurements with galactocentric distances larger than 100 arcsec achieved typically 10^{-2}. For each galaxy, the upper panels in Fig. 3 show the Sérsic profile fitted in the g and z bands with solid and dashed thin curves, respectively. The background levels are indicated with horizontal lines, and the thick curves correspond to the contributions of galaxy plus background. In Table 2 we listed the Sérsic parameters for the galaxies fitted in this work, and the corresponding background levels ($\mu_{\rm backg,0}$) in units of mag arcsec^{-2}. Regarding this latter parameter, they do not present significant differences from values expected from the ACS Exposure Time Calculator[4] in units of electrons per second for similar positions, filters, exposures, and dates to the observations. The fitted values for $\mu_{\rm backg,0}$ are also similar to those obtained by Jordán et al. (2004) for galaxies in the Virgo cluster, with similar instrumental configuration. The last column shows the integrated colours $(g-z)_{0,\rm gal}$, obtained from the integration of the Sérsic profiles. These are $\approx$0.1 mag bluer than in galaxies with similar luminosities from the Virgo cluster (Smith et al. 2013), in agreement with studies from the literature that also measured bluer colours for elliptical galaxies in low-density environments (e.g. Lacerna et al. 2016). The lower panels for each galaxy present the colour profiles in $(g-z)_0$. In some galaxies the colours are missing at large radii, this is due their surface brightness profiles fall quickly to the background level, resulting in a large noise in the colour measurement. A negative colour gradient is evident in most of the galaxies.

4.2 Effective radii of GCs

Although $r_{\rm eff}$ of GCs in some galaxies of our sample have already been measured (Jordán et al. 2005; Masters et al. 2010), those hosts presenting intermediate luminosities and located in low-density environments (programme ID 10554) lack this analysis. Moreover, the papers cited above point to the dependence of the $r_{\rm eff}$ of GCs with a mixture of properties of the host galaxy and the GCs themselves. Hence, it is interesting to corroborate whether these galaxies in our sample follow similar relations. In Table 3 the galaxies from programme 10554 are listed, together with the absolute B magnitude, the mean $r_{\rm eff}$ in the z band of GCs and their mean $(g-z)_0$ colour. We did not find a clear gradient in the mean $r_{\rm eff}$ of the GCs ($\overline{r_{\rm eff}}$) in terms of neither the host galaxy luminosity nor its colour listed in Table 2, but galaxies in this sample span a limited range for these properties. However, the results listed in Table 3 are in agreement with those in Jordán et al. (2005) for similar galaxies. There seems to exist a trend between $\overline{r_{\rm eff}}$ and mean colour for a GCS, $(g-z)_{0,\rm GCS}$, which is expected from the difference in typical $r_{\rm eff}$ for blue and red GCs (e.g. Jordán et al. 2005; Masters et al. 2010).

The upper panel of Fig. 4 shows the $(g-z)_0$ colours of the joint sample of GCs belonging to these galaxies, as a function of their $r_{\rm eff}$. The smoothed distribution suggests that bluer GCs tend to present a distribution of $r_{\rm eff}$ that reaches larger values. The lower panel presents the distribution of $r_{\rm eff}$ of the entire sample of GCs

[3]This research has made use of the NASA/IPAC Extragalactic Database (NED) which is operated by the Jet Propulsion Laboratory, California Institute of Technology, under contract with the National Aeronautics and Space Administration.

[4]http://etc.stsci.edu/etc/input/acs/imaging/

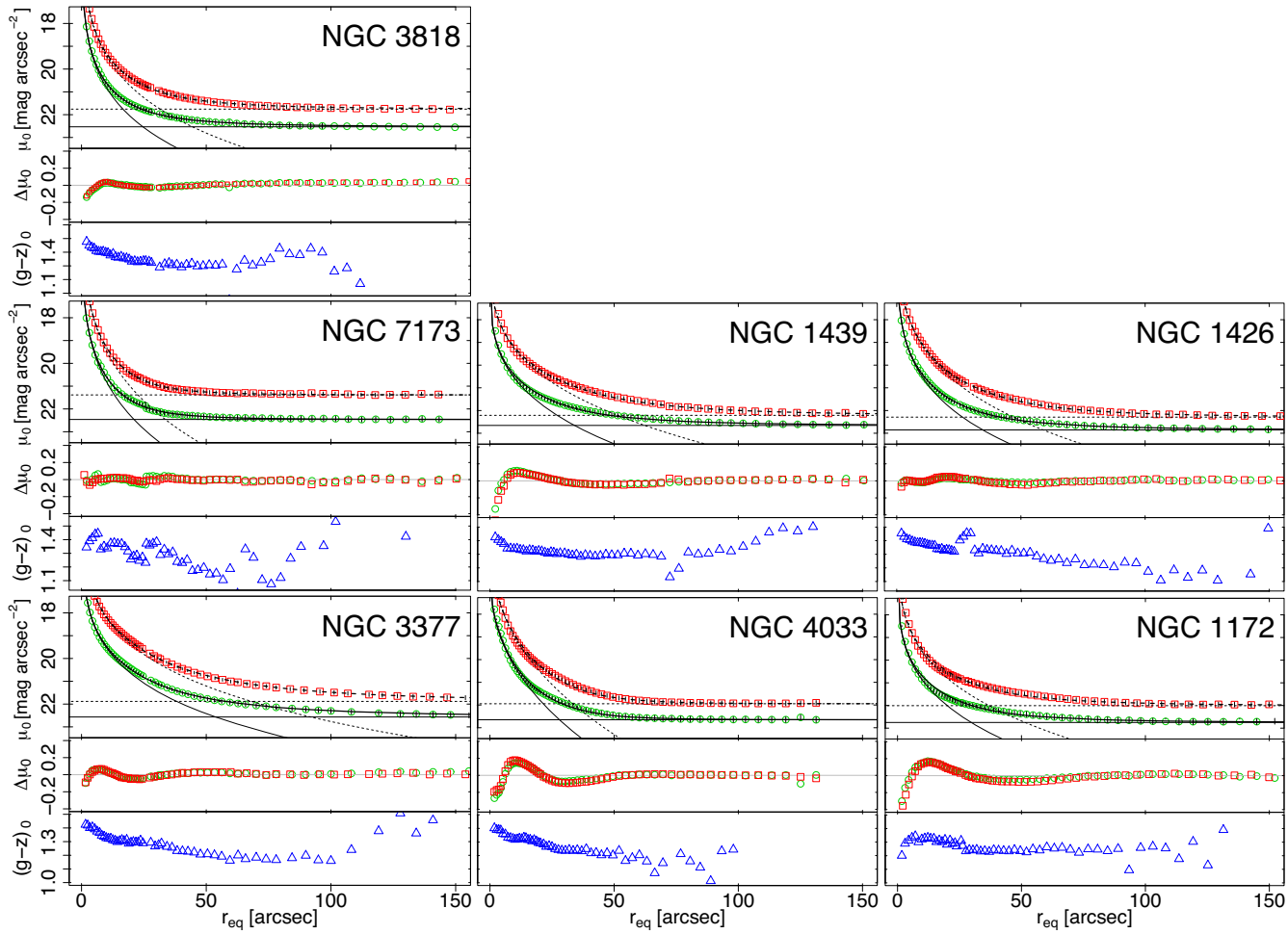

Figure 3. The upper panels show the surface-brightness profiles in g (green circles) and z (red squares) bands. The solid and dashed horizontal lines show the background level fitted in each case, the thin curves correspond to the Sérsic profile, and the thick ones to the contribution of the galaxy plus background. The fitting procedure was repeated iteratively. The middle panels represent the fit residuals, using the same symbols for each band. The lower panels correspond to the colour profile in $(g - z)_0$.

Table 2. Sérsicprofiles and background levels fitted for each galaxy, listed in decreasing B-band luminosity.

Name		$\mu_{\rm backg,0}$ (mag arcsec^{-2})	$\mu_{\rm eff,0}$	$r_{\rm eff,gal}$ (arcsec)	n	$(g-z)_{0,\rm gal}$ (mag)
NGC 3818	g	22.53	23.0 ± 0.2	31.4 ± 2.8	6.7 ± 0.4	1.31
	z	21.76	21.2 ± 0.1	23.9 ± 1.3	6.8 ± 0.4	
NGC 7173	g	22.46	21.0 ± 0.1	10.9 ± 0.6	4.4 ± 0.2	1.28
	z	21.37	19.1 ± 0.1	8.6 ± 0.3	4.1 ± 0.1	
NGC 1439	g	22.66	22.9 ± 0.1	38.1 ± 1.6	3.5 ± 0.2	1.32
	z	22.21	21.6 ± 0.1	38.8 ± 1.2	3.5 ± 0.2	
NGC 1426	g	22.84	22.2 ± 0.1	25.6 ± 0.8	4.5 ± 0.2	1.33
	z	22.29	20.7 ± 0.1	23.1 ± 0.7	4.5 ± 0.2	
NGC 3377	g	22.57	22.8 ± 0.2	59.4 ± 4.6	5.9 ± 0.3	1.18
	z	21.88	21.1 ± 0.1	47.6 ± 3.1	6.0 ± 0.3	
NGC 4033	g	22.65	20.8 ± 0.1	12.8 ± 0.4	2.5 ± 0.1	1.30
	z	21.94	19.2 ± 0.1	11.5 ± 0.4	2.4 ± 0.1	
NGC 1172	g	22.75	23.1 ± 0.2	35.4 ± 2.3	3.7 ± 0.3	1.22
	z	22.01	21.7 ± 0.1	32.4 ± 1.8	3.9 ± 0.4	

Table 3. Luminosity in the B filter for galaxies located in low-density environments studied in this paper with mean properties of their GCSs. The absolute magnitudes were obtained from the B magnitudes and the distance moduli $(m - M)$ listed in Table 4, $\overline{r_{\rm eff}}$ is the mean effective radius for all the GC candidates, and $(g - z)_{0,\rm GCS}$ their mean colours.

Name	M_B (mag)	$\overline{r_{\rm eff}}$ (pc)	$(g-z)_{0,\rm GCS}$ (mag)
NGC 3818	-20.33	3.14 ± 0.14	0.97 ± 0.02
NGC 7173	-19.96	2.69 ± 0.10	1.13 ± 0.02
NGC 1439	-19.95	3.38 ± 0.15	0.93 ± 0.03
NGC 1426	-19.65	3.09 ± 0.11	0.98 ± 0.02
NGC 3377	-19.18	2.62 ± 0.12	1.12 ± 0.02
NGC 4033	-19.11	3.35 ± 0.18	0.96 ± 0.03
NGC 1172	-18.93	2.80 ± 0.09	1.08 ± 0.01

(filled histogram), and the blue (solid line histogram) and red GCs (dashed line histogram), assuming $(g - z)_0 = 1.1$ as the colour limit between both subpopulations. As in previous studies, the blue GCs present a larger $\overline{r_{\rm eff}}$ than the red ones, 2.96 ± 0.1 and 2.55 ± 0.1 pc,

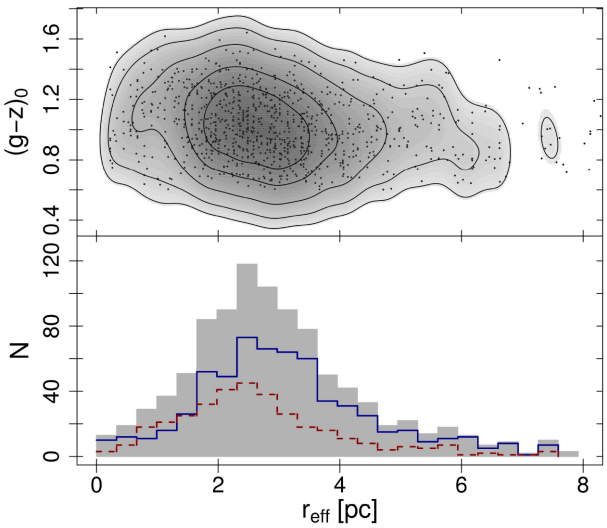

Figure 4. *Upper panel:* Smoothed distribution of $(g-z)_0$ colour of GC candidates from the joint sample as a function of their $r_{\rm eff}$. Candidates with $r_{\rm eff}$ in the range 10−20 pc, typical of extended clusters, were excluded from the figure. *Lower panel:* Distribution of $r_{\rm eff}$ for all the GC candidates (filled histogram), the blue subpopulation (solid line histogram), and the red one (dashed line histograms).

respectively. These values imply that red GCs are ≈15 per cent smaller than their blue counterparts, which is in good agreement with results from Jordán et al. (2005) for GCs in the Virgo cluster. The mean $r_{\rm eff}$ for the entire sample is 2.81 ± 0.07 pc, similar to results from other systems (e.g. Harris 2009a; Masters et al. 2010). There is a small sample of ≈20 candidates which might be classified as extended clusters (e.g. Brodie et al. 2011; Brüns & Kroupa 2012), with $r_{\rm eff}$ in the range 10−20 pc, and typical blue colours.

4.3 Radial profiles

Radial profiles of GCs are usually fitted by different mathematical expressions. Power laws (e.g. Escudero et al. 2015; Salinas et al. 2015) and de Vaucouleurs laws (e.g. Faifer et al. 2011) have been commonly used in the past, but recent papers also applied Sérsic (e.g. Usher et al. 2013; Kartha et al. 2014) and modified Hubble profiles (Binney & Tremaine 1987; Bassino & Caso 2017). In this paper we adopt the latter option:

$$n(r) = a\left(1+\left(\frac{r}{r_0}\right)^2\right)^{-b}, \qquad (5)$$

which provided accurate fits for the vast majority of GCS. This profile behaves as a power law with an exponent $2 \times b$ for large galactocentric distances and it presents a central flattening, ruled by the core radius r_0. These properties allow us to perform a direct comparison with a large sample from previous studies, and to analyse, for our galaxy sample, the paucity of GCs in the inner regions of GCSs, and its possible connection with GC erosion processes. Using the Hubble profile, we can also calculate the $r_{\rm eff,GCS}$ of the radial distribution, and compare our results with recent studies based on Sérsic profiles (e.g. Forbes 2017).

Radial profiles were fitted to projected density distributions corrected by completeness and contamination. For those galaxies belonging to programme 10554 (i.e. those in low-density environments), completeness functions were derived individually (Fig. 1), and a typical contamination density of $n_{\rm b} = 1\,{\rm arcmin}^{-2}$ was assumed. This value was calculated by Cho et al. (2012) for the same sample of galaxies from blank fields with similar galactic coordinates. The colour–magnitude diagrams obtained for our samples of GC candidates and those presented in their fig. 3 agree, which indicates that both photometries are comparable and no bias was introduced by assuming their contamination level. As mentioned above, a detailed completeness analysis was carried out for a single galaxy with intermediate luminosity belonging to the Virgo and Fornax galaxy clusters, NGC 4621 and NGC 1340, respectively. The completeness corrections for the rest of the galaxies were derived from these analysis, taking into account their mean surface-brightness in the z band for several radial ranges. For the galaxies in Virgo we adopted the Sérsic profiles derived by Ferrarese et al. (2006). For galaxies in Fornax we derived them from ACS observations obtained from MAST.

In all cases the radial binning is constant on a logarithmic scale, with a typical size of $\log_{10}\Delta r\,({\rm arcsec}) = 8$, but varying from galaxy to galaxy depending on the size of the sample of GCs. In each case the bin breaks were slightly shifted around ten times to take into account noise uncertainties, and the final parameters resulted from weighted means of the parameters fitted in the individual runs (see Table 4). Fig. 5 shows the projected radial distribution for GCSs fitted in this paper, corrected by completeness and contamination. The variation of the fitted functions due to changes in the bin breaks is represented by the grey regions. The red solid curve corresponds to the Hubble modified profile with parameters obtained from the weighted means. The contamination level n_b was calculated from fields centred on dwarf galaxies with few GC candidates, according with Peng et al. (2008).

In galaxies fainter than $M_V \approx -18$, GCSs typically present only a few dozen members (e.g. Harris, Harris & Alessi 2013), meaning radial profiles cannot be obtained without significant scatter in their parameters. Hence, we decided to stack GCSs associated with galaxies with similar luminosities, stellar masses (Peng et al. 2008) and classification in order to fit a mean radial distribution. In each case, galaxies involved in the stacking process are indicated in the corresponding panel, and labelled in Table 4 with consecutive numbers, e.g. VS# for Virgo stacked samples. The first case, VS 1 corresponds to galaxies VCC 575, VCC 1178 and VCC 1261, presenting V absolute magnitudes between −18.35 and −18.42, and stellar masses $M_\star \approx 5$–$7 \times 10^9\,M_\odot$; in VS 2 the stacked galaxies, VCC 9, VCC 437, VCC 1087, and VCC 1422, present M_V in the range −17.8 and −18.04, and $M_\star \approx 2.8$–$4 \times 10^9\,M_\odot$; the last group correspond to six galaxies with M_V between −17 and −17.5 and $M_\star \approx 1$–$2.3 \times 10^9\,M_\odot$, these are VCC 200, VCC 543, VCC 1431, VCC 1528, VCC 1871, and VCC 2019.

In total, 27 radial profiles were fitted (including the stacked galaxies), spanning absolute magnitudes from $M_B \approx -18.7$ to $M_B \approx -20.3$. The results are listed in Table 4. The columns $r_{\rm L}$ and $r_{\rm eff,GCS}$ correspond to the projected extension of the GCS calculated from our profiles and its effective radius, respectively. This latter one depends on $r_{\rm L}$, r_0, and b. The extension $r_{\rm L}$ was assumed as the galactocentric distance for which the projected density falls to 30 per cent of the contamination level, i.e. ≈0.3 arcmin^{-2}, according to the value for $n_{\rm b}$ previously indicated. This criterion has been used in past studies to define the GCS extension (e.g. Bassino & Caso 2017; Caso et al. 2017, 2019). We are aware that extrapolating radial profiles due to the limited FOV might lead to uncertainties larger than those estimated for the most extended GCS in our sample. The last three columns in Table 4 correspond to the number of members of the GCS, the effective radius of the host galaxy ($r_{\rm eff,gal}$) and its central velocity dispersion. This latter parameter was obtained

Table 4. Galaxies analysed in this paper, listed in decreasing *B*-band luminosity. Magnitudes (col. 2–5) were obtained from NED and reddening corrections from the recalibration by Schlafly & Finkbeiner (2011). Distance moduli correspond to SBF measurements listed in NED, typically from Tully et al. (2013) or Blakeslee et al. (2009). The parameters a, r_0, and b (col. 8–10) correspond to the modified Hubble profiles fitted to the GCS radial profiles. r_L, $r_{eff,GCS}$, and N_{GCs} represent the projected extension of the GCS, its effective radius and the total GC population, respectively, obtained as indicated in the text (Section 4.3). The effective radius of the host galaxies $r_{eff,gal}$ were obtained from the literature, and central velocity dispersions (σ_0) from HyperLeda database.

Name	B (mag)	V (mag)	J (mag)	K (mag)	$E_{(B-V)}$ (mag)	$(m-M)$ (mag)	a	r_0 (arcmin)	b	r_L (arcmin)	$r_{eff,GCS}$ (arcmin)	N_{GCs}	$r_{eff,gal}$ (arcsec)	σ_0 (km s^{-1})
NGC 4552	10.73	9.75	7.62	6.73	0.036	31.00	2.23 ± 0.03	0.53 ± 0.08	1.03 ± 0.09	15.8 ± 4.7	2.6 ± 1.0	984 ± 198[1]	30.0[4]	250 ± 2.9
NGC 3818	12.67	11.71	9.80	8.87	0.031	32.81	2.57 ± 0.07	0.14 ± 0.02	0.90 ± 0.03	5.4 ± 1.2	1.2 ± 0.2	240 ± −[2]	21.2[4]	193 ± 3.7
NGC 1340	11.27	10.39	8.24	7.40	0.016	31.35	1.90 ± 0.03	0.71 ± 0.12	1.22 ± 0.16	8.0 ± 2.5	1.6 ± 0.6	560 ± −[3]	39.5[4]	163 ± 3.4
NGC 4621	10.88	9.63	7.65	6.75	0.028	30.86	2.21 ± 0.03	0.32 ± 0.04	0.79 ± 0.04	25.9 ± 5.7	7.1 ± 1.3	803 ± 355[1]	46.4[4]	228 ± 3.8
NGC 4473	11.10	10.20	8.04	7.16	0.025	30.92	2.15 ± 0.05	0.42 ± 0.07	1.11 ± 0.08	9.0 ± 2.9	1.5 ± 0.4	376 ± 97[1]	24.9[4]	179 ± 2.5
NGC 1439	12.27	11.39	9.44	8.57	0.025	32.05	2.07 ± 0.04	0.29 ± 0.04	0.92 ± 0.05	7.4 ± 1.6	1.8 ± 0.4	139 ± −[2]	39.4[4]	146 ± 5.4
NGC 1426	12.29	11.39	9.57	8.67	0.014	31.82	2.23 ± 0.04	0.35 ± 0.06	1.10 ± 0.09	4.9 ± 1.5	1.04 ± 0.3	159 ± −[2]	26.1[4]	147 ± 1.9
NGC 7173	12.95	12.03	9.83	8.96	0.023	32.48	2.51 ± 0.08	0.25 ± 0.08	0.79 ± 0.10	6.0 ± 1.7	2.0 ± 0.4	208 ± −[2]	14.7[4]	201 ± 4.6
NGC 4033	12.61	11.70	9.58	8.70	0.042	31.66	2.49 ± 0.05	0.26 ± 0.03	1.27 ± 0.07	4.5 ± 1	0.6 ± 0.1	111 ± −[2]	16.1[4]	120 ± 7
NGC 1339	12.51	11.58	9.59	8.69	0.013	31.55	2.26 ± 0.04	0.43 ± 0.04	1.40 ± 0.08	4.8 ± 0.8	0.8 ± 0.1	280 ± −[3]	16.9[4]	157 ± 3
NGC 4564	12.05	11.12	8.87	7.94	0.029	31.01	2.34 ± 0.06	0.29 ± 0.04	1.35 ± 0.08	4.2 ± 1.0	0.6 ± 0.1	213 ± 31[1]	21.7[4]	156 ± 2.2
NGC 1351	12.46	11.58	9.61	8.79	0.013	31.42	2.49 ± 0.03	0.28 ± 0.02	1.14 ± 0.03	6.8 ± 0.8	0.9 ± 0.1	370 ± −[3]	25.5[4]	137 ± 2.9
NGC 1172	12.70	11.86	10.08	9.22	0.060	31.63	2.22 ± 0.03	0.51 ± 0.06	1.21 ± 0.10	5.5 ± 1.4	1.2 ± 0.2	265 ± −[2]	38.6[4]	111 ± 4.1
NGC 3377	11.24	10.38	8.29	7.44	0.030	30.13	2.13 ± 0.04	0.44 ± 0.08	1.05 ± 0.14	6.20 ± 1.9	1.5 ± 0.4	173 ± −[2]	33.7[4]	136 ± 2.3
NGC 4660	12.16	11.24	9.11	8.21	0.030	30.88	2.16 ± 0.03	0.55 ± 0.06	1.61 ± 0.12	4.6 ± 1.0	0.7 ± 0.1	205 ± 28[1]	12.8[4]	192 ± 3.2
NGC 1419	13.48	12.59	10.73	9.89	0.011	31.82	2.19 ± 0.05	0.38 ± 0.05	1.44 ± 0.11	3.7 ± 0.9	0.6 ± 0.1	160 ± −[3]	10.9[4]	117 ± 3.1
NGC 1336	13.10	12.26	10.75	9.81	0.010	31.36	2.28 ± 0.03	0.41 ± 0.04	1.24 ± 0.07	6.3 ± 1.2	1.0 ± 0.2	355 ± −[3]	–	97.7 ± 4.2
NGC 4387	12.12	13.01	10.04	9.15	0.029	31.14	1.75 ± 0.05	0.38 ± 0.05	1.50 ± 0.12	2.7 ± 0.6	0.55 ± 0.09	70 ± 10[1]	15.4[4]	100 ± 2.8
NGC 4458	12.93	12.07	10.22	9.32	0.021	31.06	2.14 ± 0.03	0.31 ± 0.04	1.54 ± 0.13	2.8 ± 0.7	0.45 ± 0.08	72 ± 12[1]	26.7[4]	97.4 ± 2.0
NGC 4434	13.03	12.15	10.07	9.21	0.019	31.15	2.22 ± 0.04	0.21 ± 0.02	1.19 ± 0.05	3.9 ± 0.6	0.58 ± 0.08	141 ± 34[1]	18.5[4]	116 ± 2.8
NGC 4623	13.24	12.36	10.31	9.47	0.020	31.17	2.26 ± 0.05	0.23 ± 0.03	1.53 ± 0.12	2.3 ± 0.5	0.34 ± 0.06	71 ± 14[1]	14.5[5]	77.0 ± 2.8
NGC 1428	13.74	−−	10.82	10.03	0.009	31.56	1.79 ± 0.05	0.34 ± 0.05	1.64 ± 0.16	1.9 ± 0.5	0.42 ± 0.08	40 ± −[3]	–	80.0 ± 10
NGC 4515	13.30	12.54	10.70	9.89	0.027	31.01	2.13 ± 0.05	0.34 ± 0.04	1.74 ± 0.15	2.4 ± 0.4	0.40 ± 0.06	81 ± 10[1]	9.5[5]	82.2 ± 2.6
NGC 1380B	13.87	12.92	10.89	10.04	0.014	31.52	2.31 ± 0.04	0.32 ± 0.03	1.37 ± 0.09	3.9 ± 0.8	0.59 ± 0.09	170 ± −[3]	–	76.6 ± 2.7
VS 1[a]	13.64	13.02	11.06	10.19	0.060	31.63	2.37 ± 0.04	0.24 ± 0.03	1.71 ± 0.16	1.0 ± 0.2	0.27 ± 0.04	24.7 ± 6[1]	13.5[5]	94 ± 15[b]
VS 2[a]	14.05	13.18	12.21	11.42	0.030	31.10	2.62 ± 0.09	0.21 ± 0.06	1.51 ± 0.20	1.8 ± 0.6	0.30 ± 0.08	34.6 ± 8[1]	24.7[5]	39 ± 4[b]
VS 3[a]	14.38	13.77	12.37	11.50	0.032	31.09	2.66 ± 0.03	0.31 ± 0.03	1.97 ± 0.15	1.5 ± 0.2	0.30 ± 0.04	22.5 ± 6[1]	21.5[5]	42 ± 3[b]

[a] These correspond to the stacked galaxies from the Virgo cluster (see the text for further details).
[b] These values correspond to the mean of the central velocity dispersions of individual galaxies.
References: [1]Peng et al. (2008), [2]Cho et al. (2012), [3]This paper, [4]Faber et al. (1989, we are aware that in this paper de Vaucouleurs profiles were used, instead of Sérsic ones), [5]Ferrarese et al. (2006)

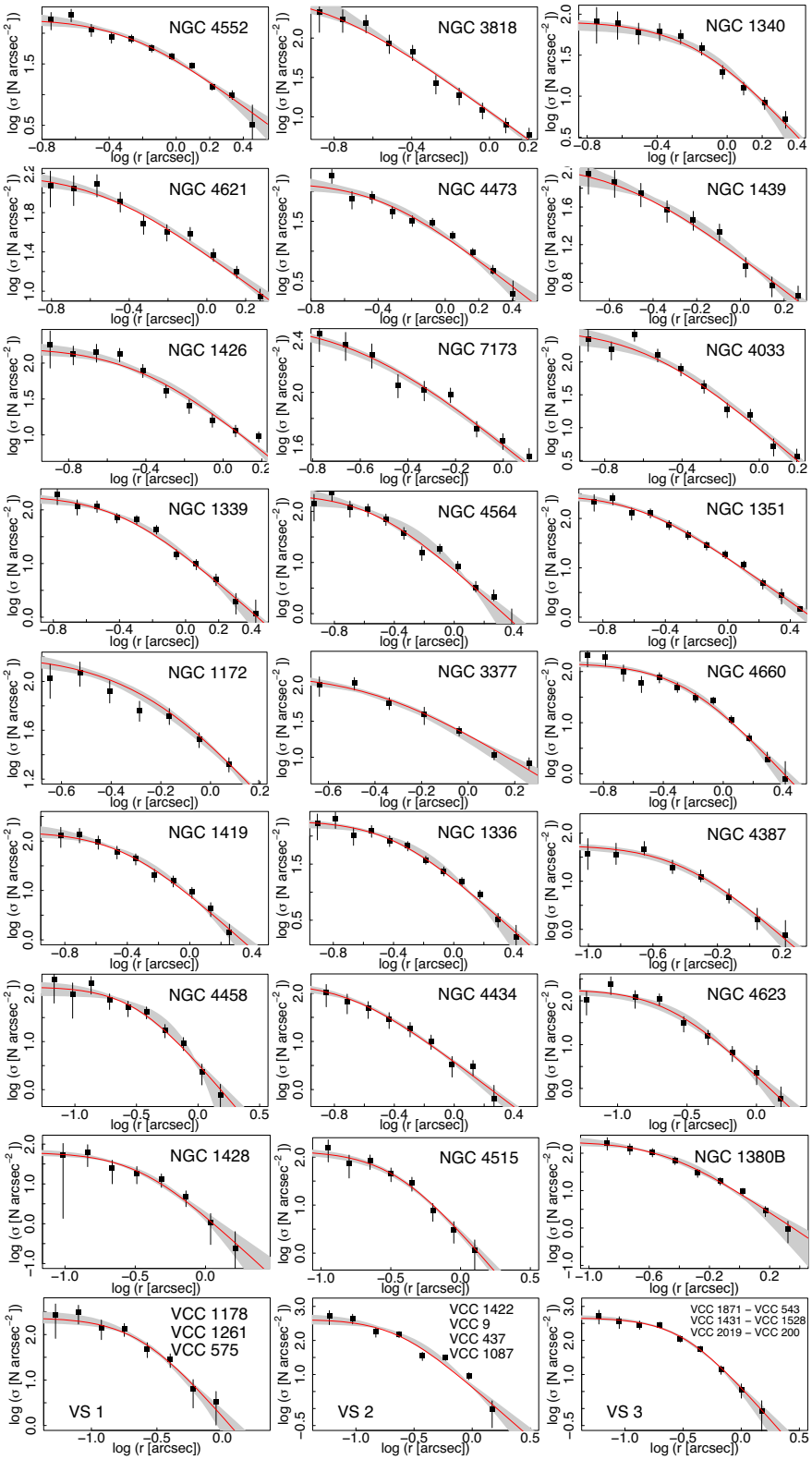

Figure 5. Projected radial distribution for GC candidates. The red solid line represents the modified Hubble profile fitted to the data. The grey region indicates the changes in the Hubble profile during individual iterations with different bin breaks (see the text for further details). The stacked low-surface-brightness Virgo galaxies are indicated with the acronym VS# and the list of galaxies contributing to the sample.

from the HyperLeda web page[5] (Makarov et al. 2014). For galaxies belonging to the Fornax cluster, the number of members of the GCS was not available in literature for the full extension of the GCS. Then, we numerically integrated the radial profiles up to the distance r_L, resulting in the number of GCs brighter than 24 mag in the z band. From the set of parameters fitted by Villegas et al. (2010) to the GCLF we calculated the fraction of GCs fainter than this magnitude limit, in order to obtain the total population of GCs indicated in the table.

In addition, we also compiled parameters from a large number of GCSs from the literature, focusing on early-type galaxies, because they are thought to have undergone a rich merger history. These galaxies are listed in Table 5, together with their magnitudes in several bands and the parameters of their GCS radial profiles. For GCSs fitted by power-law profiles, the parameter b in Table 5 corresponds to half of the power law exponent indicated in those papers. When it was possible, projected densities were obtained and Hubble profiles were fitted for those GCSs represented by Sérsic or de Vaucouleurs profiles. These cases are highlighted in Table 5, because data were not directly obtained and the uncertainties might be underestimated.

4.4 Scaling relations for GCS

4.4.1 Scaling relations with the b *parameter of the Hubble profile*

The first row in Fig. 6 shows the exponent of the Hubble profile b as a function of the logarithm of the stellar mass in units of solar masses ($M_\star$, panel A), the logarithm of the total number of GCs (N_{GC}, panel B), and the effective radius of the galaxy, expressed in kpc ($r_{eff,gal}$, panel C). The stellar masses were obtained from the luminosities in J and K bands, applying the mass-to-light ratios (M/L) derived from Bell et al. (2003) and ($B-V$) colours. Blue circles correspond to galaxies from our sample (Table 4), the other symbols represent early-type galaxies from literature (Table 5), differentiated between ellipticals (green squares) and lenticulars (red triangles).

The b parameter seems to correlate with $M_\star$ and N_{GCs}, pointing to steeper radial distributions for less massive galaxies and poorer GCSs. On the other hand, galaxies with $M_\star \gtrsim 3\times10^{10}\,M_\odot$ and $N_{GCs} \gtrsim 300$ present more extended systems, despite a large spread in the measurements. Assuming linear relations, they can be described as

$$b = 4.9\pm0.5 - 0.36\pm0.05\times X_A \quad (6)$$

represented with a solid line in panel A, with X_A being $\log_{10}(M_\star)$, and

$$b = 3.1\pm0.4 - 1.1\pm0.3\times X_B + 0.13\pm0.05\times X_B^2 \quad (7)$$

that corresponds to the solid line in panel B, with X_B being $\log_{10}(N_{GCs})$. This latter relation could be obtained from the previous one and the correlation between the size of GCS and the luminosity of the host galaxies. In fig. 6 from Harris et al. (2013) it is clear that this relation deviates from linearity when $L_K \lesssim 3\times10^9\,L_\odot$, which corresponds to the faint end of our sample. In panel C there seems to exist a correlation for galaxies with $r_{eff,gal} < 4$ kpc, for whom a linear relation is shown with a solid line, resulting in

$$b = 1.9\pm0.14 - 0.34\pm0.06\times X_C \quad (8)$$

with X_C being $r_{eff,gal}$. Galaxies with $r_{eff,gal} < 4$ kpc typically present $M_\star < 10^{11}\,M_\odot$, which is in agreement with the range of masses for which the slopes of the scaling relations change in panels D and G. There is no clear evidence for more extended galaxies, that span a wide range of b. The fit of the entire sample with a quadratic polynomial produces large uncertainties.

4.4.2 Scaling relation with the extension of the GCS

The panels in the second row show the extension of the GCS in kpc (r_L) as a function of the logarithm of $M_\star$ (panel D), the logarithm of N_{GC} (panel E), and the $r_{eff,gal}$ of the host galaxy in kpc (panel F). The symbols follow the same prescription than in previous panels. As we previously indicated, for the galaxies in our sample r_L was obtained as the galactocentric distance where the numerical density of GCs falls below the 30 per cent of the background level, and its uncertainty was calculated from the parameters of the Hubble profile fitted to the galaxy, as well as the distance estimator uncertainties, typically the 10 per cent. For galaxies from literature, uncertainties of the GCSs extension are not always provided. Hence, for the r_L we assumed the mean of the uncertainties in arcmin of our sample, plus the uncertainties in the distance estimator for each case. We find that r_L as a function of $\log_{10}(M_\star)$ can be described by a bilinear relation of the form:

$$\begin{aligned} r_L = &-99\pm10 + 12\pm2\times X_D, && M_\star \lesssim 4\times10^{10}\,M_\odot \\ &-1200\pm203 + 116\pm19\times X_D, && M_\star \gtrsim 4\times10^{10}\,M_\odot \end{aligned} \quad (9)$$

with X_D being $\log_{10}(M_\star)$. Kartha et al. (2014) proposed a single linear relation between r_L and $\log_{10}(M_\star)$ for early-type galaxies, but their sample spans stellar masses larger than the mass threshold where the slope changes. The slope of the linear relation fitted by Kartha et al. (2014) is 80.5 ± 15.7, but they obtained the stellar masses from the M/L_V ratios estimated by Zepf & Ashman (1993). The majority of the galaxies considered in this paper are ellipticals, hence the slope from Kartha et al. (2014) agrees with our fit for the massive galaxies, considering that Kartha et al. (2016) estimated that stellar masses from Zepf & Ashman (1993) are ≈1.5 times larger than those derived from Bell et al. (2003) relations. As well as for the exponent of the Hubble profile, an order-two polynomial results in an accurate description of r_L as a function of N_{GC} in logarithmic scale, resulting

$$b = 25\pm4.1 - 36\pm6.2\times X_E + 16.1\pm5.6\times X_E^2 \quad (10)$$

X_E representing the $\log_{10}(N_{GCs})$. When the functions fitted in both panels are compared, the typical residuals in panel D for galaxies more massive than $4\times10^{10}M_\odot$ double those obtained for the latter ones. Avoiding an extensive discussion about the uncertainties involved in both variables, this might imply that N_{GC} is more intrinsically related to r_L than $M_\star$ for massive galaxies.

In panel F there is a clear trend between the extension r_L and the $r_{eff,gal}$ of the galaxies, but the dispersions prevent any conclusion and further analysis on a larger sample is necessary. The dotted line corresponds to the equation (11) from Kartha et al. (2014), scaled by a factor 1.5 due the differences in the stellar masses previously indicated. The relation agrees with our data.

4.4.3 Scaling relations with the effective radius of the GCS

The third row shows the $r_{eff,GCS}$ of the GCS as a function of the $M_\star$ (panel G) and the N_{GC} (panel H), both in logarithmic scale, and the

[5] http://leda.univ-lyon1.fr

Table 5. Galaxies from the literature, listed in decreasing *B*-band luminosity. Magnitudes (col. 2–5) were obtained from NED and reddening corrections from the recalibration by Schlafly & Finkbeiner (2011). Distance moduli correspond to SBF measurements listed in NED, typically from Tully et al. (2013). The parameter *b* corresponds to the exponent of the Hubble modified profile (analogue to half of the power-law slope). $r_{\rm L}$, $r_{\rm eff,GCS}$, and $N_{\rm GCs}$ represent the projected extension of the GCS, its effective radius and the total population of GCs, respectively. The $r_{\rm eff,gal}$ of the galaxies were taken from Faber et al. (1989, please note that in this paper de Vaucouleurs profiles were used, instead of Sérsic ones). Central velocity dispersions (σ_0) were obtained from the HyperLeda database.

Name	B mag	V mag	J mag	K mag	$E_{(B-V)}$ mag	$(m-M)$ mag	b	$r_{\rm L}$ arcmin	$r_{\rm eff,GCS}$ arcmin	$N_{\rm GCs}$	$r_{\rm eff,gal}$ arcsec	σ_0 km s^{-1}
NGC 1407	10.70	9.67	7.64	6.70	0.061	32.25	0.79 ± 0.04[1]	21[1]	3.8 ± 0.2[2]	6400 ± 700[1]	71.9	266 ± 5.1
NGC 4486[a]	9.59	8.63	6.72	5.81	0.022	31.11	1.0 ± 0.08[3]	–	–	14660 ± 891[4]	81.3	323 ± 4.3
NGC 4406[a]	9.83	8.9	7.01	6.10	0.028	31.26	0.62 ± 0.03[5]	–	5.8 ± 0.1[6]	$2900 \pm -$[5]	35.2	231 ± 2.6
NGC 1395	10.55	9.59	7.83	6.89	0.021	31.88	0.68 ± 0.02[7]	24[7]	–	6000 ± 1100[7]	45.4	240 ± 4.3
NGC 4649[a]	9.81	8.84	6.67	5.74	0.025	31.08	0.69 ± 0.02[8]	–	6.1 ± 2.1[8]	4690 ± 980[8]	66.1	331 ± 4.6
NGC 4594[a]	8.98	8.00	5.89	4.96	0.045	30.26	0.93 ± 0.04[5]	19[5]	5.9 ± 0.4[6]	$1900 \pm -$[5]	–	226 ± 3.3
NGC 4374	10.09	9.11	7.12	6.22	0.036	31.34	0.55 ± 0.06[9]	–	–	4301 ± 1201[4]	52.5	278 ± 2.4
NGC 3962	11.62	10.67	8.56	7.67	0.039	32.80	0.91 ± 0.07[10]	–	–	854 ± 98[10]	34.4	220 ± 13
NGC 5813[a]	11.45	10.46	8.34	7.41	0.05	32.50	1.07 ± 0.03[11]	13[11]	3.9 ± 0.3[11]	2900 ± 400[11]	57.5	236 ± 3.4
NGC 720[a]	11.16	10.18	8.18	7.27	0.014	32.17	1.21 ± 0.05[2]	10[2]	2.0 ± 0.3[2]	1489 ± 96[2]	39.5	239 ± 4.6
NGC 1399	10.6	9.59	7.21	6.31	0.012	31.53	0.81 ± 0.05[12]	45[12]	–	6450 ± 700[13]	42.4	332 ± 5.3
NGC 3311	12.65	11.65	8.97	8.10	0.076	33.55	1.02 ± 0.04[14]	9[14]	–	16500 ± 2000[14]	–	185 ± 6.3
NGC 2768[a]	10.84	9.87	7.93	6.99	0.044	31.73	1.25 ± 0.09[2]	10[2]	1.7 ± 0.2[2]	744 ± 68[2]	63.1	185 ± 2.8
NGC 4636[a]	10.0	9.5	7.31	6.42	0.027	30.86	0.88 ± 0.05[15]	14[15]	–	4200 ± 120[15]	89.1	199 ± 2.7
NGC 3923[a]	10.80	9.80	7.42	6.50	0.071	31.64	0.62 ± 0.04[8]	–	0.6 ± 0.2[8]	4580 ± 820[8]	53.3	246 ± 4.9
NGC 4365	11.0	9.6	7.5	6.6	0.021	31.82	0.67 ± 0.05[16]	–	6.1 ± 1.2[2]	6450 ± 110[16]	52.5	250 ± 2.6
NGC 6411	12.79	11.85	10.02	9.13	0.048	33.58	1.07 ± 0.09[17]	5[17]	–	700 ± 45[17]	26.7	183 ± 4.6
NGC 4762	11.1	10.3	8.2	7.3	0.021	31.82	0.93 ± 0.0117	5[11]	1.4 ± 0.4[11]	270 ± 30[11]	43.7	141 ± 4.1
NGC 7507	11.36	10.38	8.20	7.29	0.044	31.95	1.23 ± 0.05[18]	7[18]	–	350 ± 50[18]	31.4	217 ± 2.7
NGC 1404	10.97	10.00	7.77	6.82	0.010	31.53	$0.85 \pm - -$[19]	4[20]	–	725 ± 145[20]	26.7	230 ± 3.8
NGC 4494	10.71	9.83	7.90	6.99	0.018	31.14	0.85 ± 0.10[21]	10[21]	–	392 ± 49[21]	49.0	148 ± 2.6
NGC 2865	12.57	11.66	9.36	8.46	0.074	32.95	0.94 ± 0.08[10]	–	–	410 ± 8[10]	11.7	171 ± 2.8
NGC 1380	10.87	9.93	7.77	6.86	0.017	31.23	0.81 ± 0.05[22]	3[22]	–	560 ± 30[22]	–	215 ± 4.6
NGC 3268	12.5	11.45	9.12	8.15	0.098	32.83	0.9 ± 0.05[23]	13[23]	–	8200 ± 800[23]	36.1	229 ± 16
NGC 3258	12.5	11.5	9.25	8.31	0.077	32.71	0.9 ± 0.05[23]	13[23]	–	8000 ± 800[23]	27.4	261 ± 9.8
NGC 5866	10.74	9.89	7.83	6.87	0.013	30.93	0.88 ± 0.05[11]	10[11]	3.1 ± 0.7[11]	340 ± 80[11]	36.3	162 ± 4.7
NGC 6861	12.1	11.1	8.66	7.71	0.052	32.28	0.80 ± 0.02[24]	10[24]	–	3000 ± 300[24]	22.8	387 ± 16
NGC 821[a]	11.67	10.68	8.80	7.90	0.097	31.83	1.24 ± 0.26[25]	4[25]	–	320 ± 45[25]	39.8	198 ± 2.8
NGC 3115	9.87	8.9	6.78	5.88	0.044	29.93	0.98 ± 0.06[8]	–	–	546 ± 80[8]	36.1	260 ± 3
NGC 3379[a]	10.24	9.28	7.17	6.27	0.022	30.25	0.71 ± 0.07[5]	11[5]	–	$270 \pm -$[5]	39.8	202 ± 1.8
NGC 1052[a]	11.41	10.47	8.37	7.45	0.023	31.42	1.04 ± 0.07[26]	3[26]	–	400 ± 45[26]	36.9	208 ± 3.9
NGC 5128	7.84	6.84	4.98	3.94	0.101	27.82	1 ± 0.1[27]	–	–	$1550 \pm -$[28]	–	103 ± 6.2
NGC 4278[a]	11.09	10.16	8.09	7.18	0.026	30.93	0.88 ± 0.02[29]	20[29]	2.8 ± 0.5[29]	1378 ± 200[29]	31.6	237 ± 4.5
NGC 1387	11.68	10.69	8.44	7.43	0.011	31.43	1.2 ± 0.15[30]	3[30]	–	390 ± 27[30]	–	167 ± 12
NGC 1379	11.80	10.91	9.08	8.24	0.012	31.54	1.3 ± 0.25[30]	3[30]	–	225 ± 23[30]	42.4	117 ± 2.2
NGC 1427	11.77	10.86	9.03	8.14	0.011	31.46	1 ± 0.1[31]	5[31]	–	470 ± 40[31]	32.9	155 ± 2.8
NGC 7332	12.02	11.11	8.98	8.07	0.033	31.66	0.63 ± 0.07[32]	2[32]	0.4 ± 0.1[33]	175 ± 15[32]	17.4	128 ± 3.3
NGC 4754	11.5	10.6	8.31	7.41	0.03	31.04	0.71 ± 0.07[11]	3[11]	2.6 ± 0.9[11]	115 ± 15[11]	31.6	177 ± 3
NGC 1374	12.00	11.08	9.05	8.16	0.012	31.46	1.15 ± 0.1[30]	2[30]	–	360 ± 17[30]	30.0	179 ± 3.3
NGC 2271	13.16	–	8.68	9.69	0.104	32.53	1.09 ± 0.09[10]	–	–	562 ± 9[10]	–	148 ± 20
NGC 1400	11.92	10.96	8.75	7.81	0.062	31.06	0.58 ± 0.10[34]	3[34]	–	922 ± 280[35]	37.8	246 ± 3.4
NGC 3384	11.00	9.9	7.7	6.8	0.026	30.01	0.65 ± 0.09[11]	5[11]	2.4 ± 1.3[11]	120 ± 30[11]	32.3	144 ± 2.5
NGC 7457	12.09	11.20	9.11	8.19	0.047	30.41	0.91 ± 0.06[36]	3[36]	–	210 ± 30[36]	36.3	68 ± 3.5

[a] The power-law slopes indicated in the table were obtained by fitting the density profiles published in the corresponding paper.

References: [1]Forbes et al. (2011), [2]Kartha et al. (2014), [3]Harris (2009b), [4]Peng et al. (2008), [5]Rhode & Zepf (2004), [6]Kartha et al. (2016), [7]Escudero et al. (2018), [8]Faifer et al. (2011), [9]Gómez & Richtler (2004), [10]Salinas et al. (2015), [11]Hargis & Rhode (2012), [12]Bassino et al. (2006a), [13]Dirsch et al. (2003), [14]Wehner et al. (2008), [15]Dirsch, Schuberth & Richtler (2005), [16]Blom, Spitler & Forbes (2012), [17]Caso et al. (2019), [18]Caso et al. (2013), [19]Capuzzo-Dolcetta & Mastrobuono-Battisti (2009), [20]Forbes et al. (1998), [21]Foster et al. (2011), [22]Kissler-Patig et al. (1997), [23]Caso et al. (2017), [24]Escudero et al. (2015), [25]Spitler et al. (2008), [26]Forbes & Forte (2001), [27]Harris, Harris & Geisler (2004), [28]Harris et al. (2006), [29]Usher et al. (2013), [30]Bassino, Richtler & Dirsch (2006b), [31]Forte et al. (2001), [32]Young, Dowell & Rhode (2012), [33]Hudson & Robison (2018), [34]Forbes et al. (2006), [35]Perrett et al. (1997), [36]Hargis et al. (2011).

$r_{\rm eff,gal}$ of the host galaxy (panel I). As in panel D, we fitted a bilinear relation:

$$\begin{aligned} r_{\rm L} = &-22.5 \pm 6.8 + 2.6 \pm 0.7 \times X_{\rm G}, \quad M_\star \lesssim 4 \times 10^{10}\,{\rm M}_\odot \\ &-315 \pm 67 + 30.3 \pm 6.1 \times X_{\rm G}, \quad M_\star \gtrsim 4 \times 10^{10}\,{\rm M}_\odot \end{aligned} \tag{11}$$

with $X_{\rm G}$ being $\log_{10}(M_\star)$, plotted with black solid lines. The dotted grey curve represents the relation derived by Forbes (2017) for early-type galaxies, while the dash–dotted grey curve corresponds to a sample of early- and late-type galaxies from Hudson & Robison (2018). Both relations seem to underestimate the $r_{\rm eff,GCS}$ of the GCS

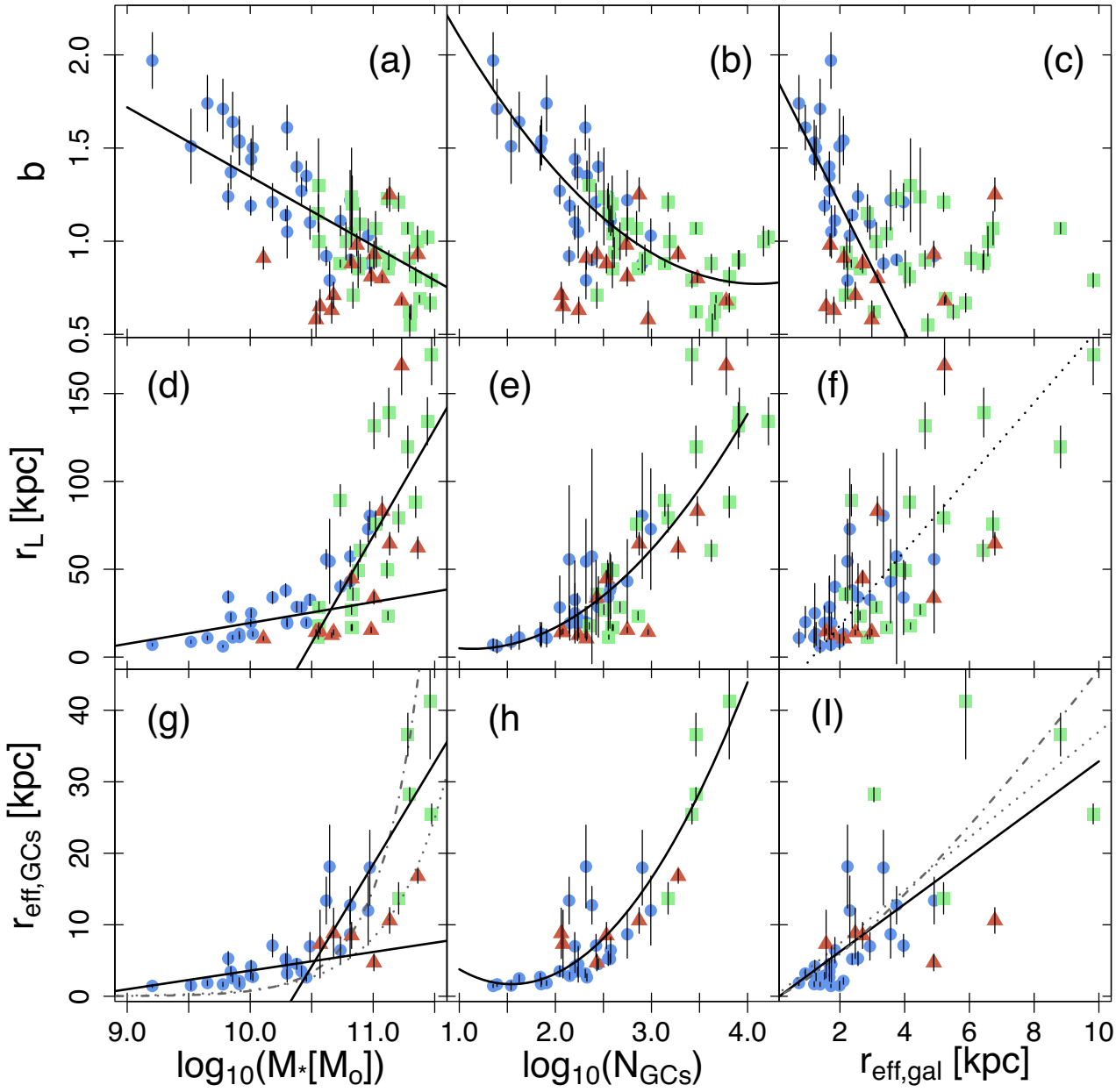

Figure 6. The exponent of the modified Hubble profile (b), the extension of the GCS ($r_{\rm L}$) and its effective radius ($r_{\rm eff,GCS}$), as functions of the logarithm of the stellar mass ($M_\star$), the logarithm of the number of GCs ($N_{\rm GCs}$), and the effective radius of the host galaxy ($r_{\rm eff,gal}$). Blue circles represent the galaxies analysed in this paper (Table 4), green squares and red triangles, respectively, indicate ellipticals and lenticulars from the literature (Table 5). Solid curves show relations fitted in this paper, dotted, and dash–dotted curves correspond to literature results (Kartha et al. 2014; Forbes 2017; Hudson & Robison 2018). See text for further details.

for the low stellar mass galaxies. Besides, the relations deviate significantly for stellar masses above $10^{10}\,{\rm M}_\odot$, with observations showing a large spread at fixed $M_\star$. In panel H the $r_{\rm eff,GCS}$ of the GCS is fitted by a quadratic polynomial of the form:

$$b = 17 \pm 6.1 - 20.6 \pm 5.7 \times X_{\rm H} + 6.8 \pm 1.2 \times X_{\rm H}^2 \qquad (12)$$

with $X_{\rm H}$ being $\log_{10}(N_{\rm GC})$. Although there is a clear dependence in the calculus of both parameters, it is worth to emphasize the tight correlation between them, pointing to the richness of the GCS as the main factor to determine its extension. On the other hand, panel I shows the $r_{\rm eff,GCS}$ of the GCS against the $r_{\rm eff,gal}$ of the host galaxy. The solid curve corresponds to a linear relation fitted to the data.

$$b = 0.4 \pm 2 + 3.3 \pm 0.55 \times X_{\rm I}. \qquad (13)$$

The dash–dotted grey curve corresponds to the relation derived by Hudson & Robison (2018), while the dotted grey curve represents the mean ratio for both parameters from Forbes (2017). Both expressions are in agreement with our fit, considering the lack of $r_{\rm eff,GCS}$ measurements for many GCSs in massive galaxies, and the dispersion of the available ones. These limitations prevent further conclusions.

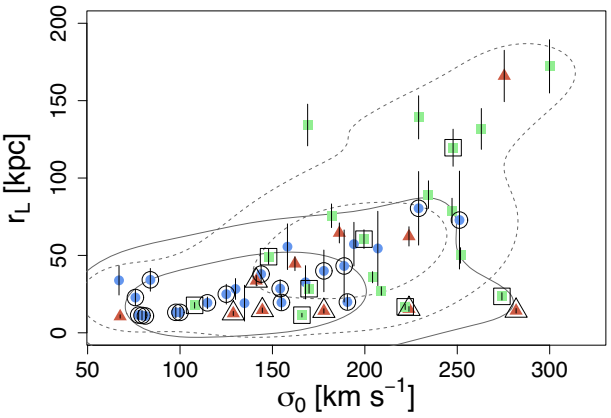

Figure 7. The extension of the GCS r_L as a function of the central velocity dispersion σ_0. The symbols follow the same prescription than previous figures. Framed ones highlight the satellites of more massive galaxies. The solid contours are indicative of the locus of the satellites, while the dashed ones correspond to central galaxies.

4.4.4 *Comparison with other parameters*

In Fig. 7 we explore the differences in the extension of the GCS r_L as a function of the central velocity dispersion σ_0 for the galaxies listed in Tables 4 and 5. The symbols follow the same prescription that previous figures, with framed ones representing satellite galaxies. This classification was based on the information indicated in the papers that analysed their corresponding GCSs. We are aware of the effect of possible misclassifications. The contours are only indicative of the locus that satellites (solid curves) and central galaxies (dashed curves) occupy. In the latter ones r_L shows a correlation with σ_0, but it is nearly invariant for satellites. There are four GCSs labelled as satellites that follow the central galaxies correlation. Two of them come from the literature sample and correspond to NGC 4636 and NGC 4649, giant ellipticals from the Virgo cluster that dominate respective cluster subgroups, present very populated GCSs (see Table 5) and extended dark matter haloes (e.g. Das et al. 2011; Schuberth et al. 2012). The other two galaxies are VC1903 and VCC1632, which also belong to the Virgo cluster. Their GCSs contain around a thousand members and, as we previously indicated, the derived value of r_L is only indicative, because it largely exceeds our FOV.

We lack of characterizations of the dark matter haloes for the galaxies in our sample, hence direct comparison between the halo mass or virial radius and the parameters of the GCS is not possible. Instead we applied a statistical point of view. We selected from the SMDPL simulation those haloes with K luminosities in the same range as the galaxies analysed in this paper. Then we projected their density distribution, described by a Navarro, Frenk & White profile (hereafter, NFW profile Navarro, Frenk & White 1996), on the Cartesian xy plane. Sérsic profiles provided an accurate fit to the resulting projected distributions. The red solid line in the upper panel of Fig. 8 corresponds to the r_{200} radius, defined as the galactocentric distance where the volumetric density equals 200 times the critic density at $z = 0$. The symbols indicate the extent of the GCS (r_L), scaled to the distribution of r_{200} of the haloes for comparison purposes. There seems to be an agreement in the behaviour of both parameters as a function of M_K. The scaling factor results $r_{200} = f_{200} \times r_L$ with $f_{200} = 8.5 \pm 0.5$. The symbols follow the same prescription that in previous figures. The smoothed distribution of $r_{\rm eff,halo}$ of the haloes in terms of M_K is shown in the

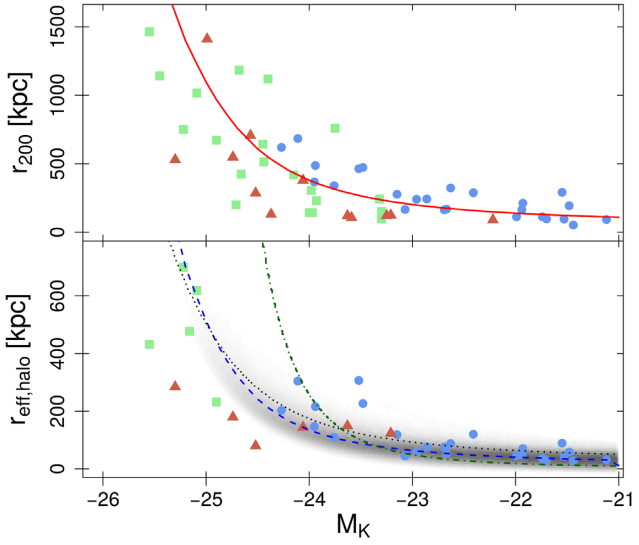

Figure 8. *Upper panel:* The red solid line corresponds to the distribution of r_{200} for the haloes from SMDPL as a function of the K absolute magnitude assigned by the HOD method, and the symbols are the r_L of the GCS, scaled to fit this latter one by a factor f_{200}. *Lower panel:* Smoothed distribution of the $r_{\rm eff,halo}$ fitted with a Sérsic profile to the projected haloes from the SMDPL simulation. The dashed curve indicates the mean values of $r_{\rm eff,halo}$ as a function of M_K. Filled symbols represent the $r_{\rm eff,GCS}$ of the GCS, scaled to the $r_{\rm eff,halo}$ distribution by a factor $f_{\rm eff}$. The dotted curve shows the relation between the size of galaxies and the virial radius derived by Kravtsov (2013), as represented in Forbes (2017), but scaled by the factor $f_{\rm eff}$ to follow the $r_{\rm eff,GCS}$ in our plot. The dash–dotted curve corresponds to the relation fitted by Hudson & Robison (2018) between the $r_{\rm eff,GCS}$ and the r_{200}, applying the same scaling factor $f_{\rm eff}$.

lower panel of Fig. 8, and its mean values are represented by the blue dashed curve. The filled symbols indicate the $r_{\rm eff,GCS}$ of the systems with available measurements, scaled to the $r_{\rm eff,halo}$ of the haloes. In this case the scaling factor was fitted to the dashed line, on the basis of a possible correlation between the parameters, resulting that $r_{\rm eff,halo} = f_{\rm eff} \times r_{\rm eff,GCS}$, with $f_{\rm eff} = 16.7 \pm 2.3$. The distribution of scaled $r_{\rm eff,GCS}$ of the GCS seems to follow the distribution of $r_{\rm eff,halo}$ of the haloes, despite a larger sample of bright galaxies would provide a more accurate result. This gives confidence to the assumption that the $r_{\rm eff}$ of haloes and GCSs are correlated.

The dotted curve shows the relation derived by Kravtsov (2013) for the galaxy size as function of the virial radius, scaled by 3.7 to consider the mean ratio between galaxies and GCS sizes Forbes (2017), and by $f_{\rm eff}$. The relation is in agreement with the $r_{\rm eff,GCS}$ of the GCS. The dash–dotted curve corresponds to the relation between the r_{200} radius and the $r_{\rm eff,GCS}$ of the GCS derived by Hudson & Robison (2018), once again scaled by $f_{\rm eff}$, but it seems to overestimate $r_{\rm eff}$ for galaxies brighter than $M_K = -23.5$ mag.

GCS in elliptical galaxies usually present a flattened radial distribution, less peaked in the inner arcsecs than the galaxy light profile (e.g. Harris & Racine 1979; Capuzzo-Dolcetta & Mastrobuono-Battisti 2009; Caso et al. 2017), even when the variation in the completeness with the galactocentric distance, is taken into account (e.g. Bassino & Caso 2017). In Fig. 9 the ratio between the core radius r_0 from the Hubble profile and the $r_{\rm eff,gal}$ of the galaxy is plotted as a function of the logarithm of the $M_\star$ for the galaxies in our sample. In this case we avoid the comparison with literature data based in two reasons, (i) the treatment of the completeness as a function of the galactocentric radius results in more accurate

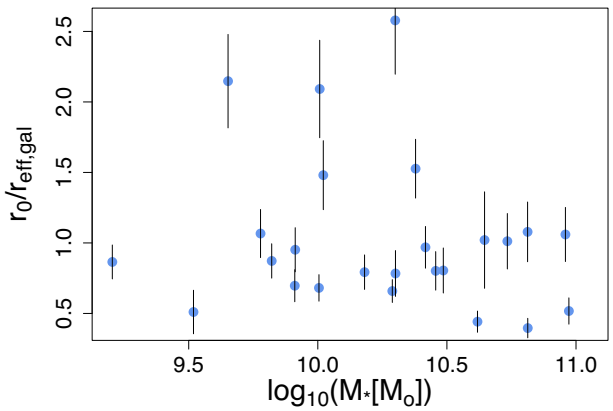

Figure 9. Ratio between the core radius from the Hubble profile (r_0) and the $r_{\rm eff,gal}$ of the host galaxy, as a function of $M_\star$. Points with large ratio might be overestimated due to small measurements of $r_{\rm eff,gal}$.

measurements of GCs projected densities, particularly for bright ellipticals, and the lack of this analysis might lead to significant differences in the inner region of the radial profile, (ii) Brockamp et al. (2014) studied the dissolution processes ruling the GC erosion with numerical simulations, pointing that the core size depends on the threshold mass for the GCs, because low-mass GCs are more affected by disruption processes than the most massive ones. Then, the faint limit in magnitude achieved in the observations is important, and the inclusion of results from different instruments and photometric depth would introduce unnecessary noise.

The majority of GCSs in our sample present $r_0/r_{\rm eff,gal} \approx 1$, which resembles the results from Brockamp et al. (2014) for the models MOD2 and MOD3, with $M_\star \approx 1$–$3 \times 10^{11}\,{\rm M}_\odot$. There are few galaxies presenting ratios above 1.5, but in all cases they present lower $r_{\rm eff,gal}$ than galaxies with similar stellar masses, pointing that large ratios are due to the underestimation of this latter parameter. These galaxies are NGC 4660, NGC 4515, and NGC 1419. Brockamp et al. (2014) indicate that the fraction might be lower for the most massive and extended galaxies, but our sample does not allow us to test it.

5 DISCUSSION

Rodríguez-Puebla et al. (2016) analysed the population of dark matter haloes from the cosmological simulations Bolshoi-Planck and Multidark-Planck (Klypin et al. 2016). They found that the distribution of concentration index at $z = 0$ depends on the virial mass, becoming more extended for more massive haloes. Moreover, in the surface-brightness profiles in early-type galaxies the Sérsic index n and the $r_{\rm eff,\,gal}$ correlates with luminosities (e.g. Calderón et al. 2015), implying that galaxies with moderate luminosity are more compact than the brightest ones. Under the assumption that GCSs are related with the mass distribution of the host galaxy, it is expected to obtain steeper radial distributions when the galaxies become less massive.

Kartha et al. (2014) compared the properties of GCSs for a sample of early and late-type massive galaxies, with the host galaxy stellar mass, resulting in a linear relation with $\log_{10}(M_\star)$, that is in agreement with our results for galaxies with $M_\star \gtrsim 4 \times 10^{10}\,{\rm M}_\odot$ when a scaling relation due to the different sources of the M/L relations (Kartha et al. 2016) is considered. The change in slope for lower masses might be related with the stellar mass–size relation for galaxies, that flattens for central galaxies (e.g. Shen et al. 2003; Shankar et al. 2014). Shankar & Bernardi (2009) indicated that the late evolution of the most massive galaxies in rich environments, mainly driven by minor mergers, might explain the gradual steepening of the size-mass relation for larger luminosities. We are aware that most of the galaxies in our sample are satellites in dense environments like the Virgo and Fornax clusters, but Huertas-Company et al. (2013) showed that central and satellite early-type galaxies follow a similar stellar mass–size relation. Similar results were found by Spindler & Wake (2017), who claimed that it cannot be ruled out that environmental processes may modify the size and mass for a given galaxy. In fact, they propose to the central velocity dispersion (σ_0) as invariant variable to changes due to environmental processes. They found that, at fixed σ_0, quiescent central galaxies are larger and more massive than their satellite counterparts. This is expected considering that satellite galaxies, moving through a high density environment like the intracluster medium, should experience a ram pressure that might strip its gas, leading to the reduction of the star formation and a subsequent reduced size (e.g. Kapferer et al. 2009). Taking into account that GCSs are typically more extended than the field population of the galaxy, it is expected for environmental processes to also affect them, particularly their extension ($r_{\rm L}$). Central velocity dispersions tend to be invariant to growth by minor mergers, Bezanson, van Dokkum & Franx (2012) found that the internal dynamics of quiescent galaxies, in the high central velocity dispersion regime, remains roughly unchanged with time. The authors point to a rapid quench, becoming more efficient with the increase of the velocity dispersion. Minor mergers should have played a relevant role in the mass increase in later stages, that in central ellipticals might represent an important fraction of their mass at $z = 0$ (van Dokkum et al. 2010). The mergers that increase the stellar mass of the central galaxy also provide GCs that enlarge the pre-existing population, in detriment of satellites which hardly experienced merging episodes.

The halo mass–size relation for galaxies has also been studied by Kravtsov (2013) and Charlton et al. (2017). The latter ones estimated halo mass from weak lensing analysis and found a differential measurement of the halo mass–size relation at fixed stellar mass, in the form of a power law. Although the fitted exponents vary with stellar mass, the average values differ between blue and red galaxies, described in their paper as primarily star-forming discs and quiescent ellipticals, respectively. Hudson & Robison (2018) derived a correlation between the $r_{\rm eff,GCS}$ of the GCS and the halo extension and mass for a sample of early and late-type galaxies. Although the previously mentioned evolutionary differences between central and satellite galaxies might play a role, they found that GCSs with larger $r_{\rm eff,GCS}$ occupy larger and more massive haloes.

The stellar mass at which the slope changes in our equation (8) matches with that corresponding to the maximum of the ratio $M_\star/M_{\rm halo}$ from numerical simulations (Behroozi, Conroy & Wechsler 2010; Moster et al. 2010). Cora et al. (2018) differentiated satellite and main haloes, for halo masses below $\approx 10^{12}\,{\rm M}_\odot$ (i.e. $M_\star \approx 3 \times 10^{10}\,{\rm M}_\odot$) they found that central galaxies inhabit more massive haloes than satellites at fixed stellar mass. This might be understood in terms of the mass loss in subhaloes, mainly due to dynamical friction, tidal stripping and tidal heating (e.g. Gan et al. 2010). Moreover, the calculus of the tidal radius $r_{\rm t}$ in satellite galaxies after the accretion epoch has to reflect the fact that the satellite galaxy is bound to more massive halo, instead of r_{200}. In a simplified approach, the $r_{\rm t}$ is reached when the gravitational acceleration towards the satellite centre equals the tidal acceleration from the host potential. Although a more accurate treatment should

involve the phase space distribution of the satellite particles (e.g. Kampakoglou & Benson 2007), the qualitative idea that the virial radius of a halo is shorten afterwards it is accreted by a more massive one remains valid. The majority of the galaxies in our sample are indeed satellites in density environments like the Virgo and Fornax clusters, and hence their haloes should have experienced this environmental effects.

It is scarcely a novelty that the concentration of the radial distribution of GCS (represented by the parameter b), as well as its r_L and $r_{eff,GCS}$, are related with the richness of the GCS. This latter property is closely connected to the merger history of the host galaxy, responsible for the mass accretion but also for the built up of the GCS through major starburst driven by merging episodes (e.g. Muratov & Gnedin 2010; Li & Gnedin 2014) and accretion of GCs (Forbes et al. 2011; Amorisco 2019). Moreover, Kruijssen (2015) pointed that the environmental conditions that favour GCs formation also lead to their tidal disruptions at early stages in their evolution, and that subsequent mergers are needed to eject them to the host galaxy halo, improving their survival ratio. Although there is a large dispersion, reviews on the subject seem to confirm this connection with the stellar (e.g. Harris et al. 2013) and virial masses (e.g. Hudson et al. 2014) for early-type galaxies. The dispersion in the relations might be ruled by the environmental conditions that affect the formation and evolution of the GCS in cluster-like environments (e.g. Peng et al. 2008) as well as in the field (e.g. Salinas et al. 2015).

Environmental conditions increase the disruption rate of GCs in the inner regions of galaxies, leading to the flattening in their radial profiles. Capuzzo-Dolcetta & Mastrobuono-Battisti (2009) proposed dynamical friction as the mechanism behind this GC erosion, but it has been ruled out in more recent papers (Brockamp et al. 2014). These authors tested the efficiency of different dissolution processes involved in the GC erosion through numerical simulations. They found that GCs density profiles are typically flattened in less than a Hubble time. The resulting cores depend on the mass and effective radius of the galaxy, but radial anisotropies of the GCS might also play a main role. Other studies focused on the evolution of Galactic GCs also point to the relevance of the mass-loss rate when GCs are subject to strong tidal fields close to the centre of the Galaxy (e.g. Webb et al. 2014; Madrid et al. 2017). The accurate analysis of the inner density distribution of GCS might provide relevant information about the mechanisms ruling the kinematical behaviour of the field population in the inner region of the galaxies.

6 SUMMARY

We performed the photometry of HST/ACS archive observations of several intermediate luminosity galaxies located in low-density environments. It was supplemented with available photometries of GCSs from the Virgo and Fornax clusters, resulting in a sample of almost 30 GCS for whom we fitted their radial profiles. Additional literature studies were compiled to enlarge the sample. We summarize our conclusions in the following.

(i) For the galaxies in low-density environments, we obtained the effective radii of their GCs. Blue GCs are more extended than red ones, and mean values are in agreement with previously published results. The reduced luminosity range spanned by these galaxies does not allow us to observe any trend between the mean effective radii and the stellar mass.

(ii) Hubble modified profiles provide an accurate fit for the entire sample of GCSs. The exponent of the power law correlates with the stellar mass of the host galaxy and the number of GCs, being steeper for low-mass galaxies. The relation with the effective radius of the galaxy is not clear at the luminous end. This suggests that the concentration of the GCS depends on the general properties directly related with the mass growth of the galaxy.

(iii) The extension of the GCS also correlates with the stellar mass, the number of GCs, and the effective radius of the galaxy. In the first case, the relation flattens for galaxies with stellar masses below $4 \times 10^{10}\,M_{\odot}$. Due to the commonly known non-linear relation between the stellar mass and the number of GCs, the correlation with this later property is soften and a quadratic curve is an accurate description.

(iv) The effective radius of the GCS correlates with the effective radius of the host galaxy, as indicated in previous studies, but with a large dispersion. The comparison with the stellar mass and the number of GCs shows a similar behaviour than that described for the GCS extension.

(v) The extension of the GCS of central galaxies seems to correlate with the central velocity dispersion, but it presents a distinctive behaviour for satellites. We interpret this in the context of the different mass accretion history of the two groups of galaxies.

(vi) From the statistical comparison with numerical simulations, the effective radius of the GCS scales with the projected effective radius of the haloes, and the extension of the GCS scales with their virial radius.

(vii) The size of the core of the Hubble modified profile for GCS correlates with the effective radius of the galaxy, in agreement with results from numerical simulations for low- and intermediate-mass ellipticals.

ACKNOWLEDGEMENTS

This work was funded with grants from Consejo Nacional de Investigaciones Científicas y Técnicas de la República Argentina, Agencia Nacional de Promoción Científica y Tecnológica, and Universidad Nacional de La Plata (Argentina). This research has made use of the NASA/IPAC Extragalactic Database (NED) which is operated by the Jet Propulsion Laboratory, California Institute of Technology, under contract with the National Aeronautics and Space Administration. We thank the referee for a constructive report that helped to improve this paper. We acknowledge the usage of the HyperLeda database.

REFERENCES

Alabi A. B. et al., 2017, MNRAS, 468, 3949
Amorisco N. C., 2019, MNRAS, 482, 2978
Bassino L. P., Caso J. P., 2017, MNRAS, 466, 4259
Bassino L. P., Faifer F. R., Forte J. C., Dirsch B., Richtler T., Geisler D., Schuberth Y., 2006a, A&A, 451, 789
Bassino L. P., Richtler T., Dirsch B., 2006b, MNRAS, 367, 156
Bassino L. P., Richtler T., Dirsch B., 2008, MNRAS, 386, 1145
Behroozi P. S., Conroy C., Wechsler R. H., 2010, ApJ, 717, 379
Bell E. F., McIntosh D. H., Katz N., Weinberg M. D., 2003, ApJS, 149, 289
Bertin E., Arnouts S., 1996, A&AS, 117, 393
Bezanson R., van Dokkum P., Franx M., 2012, ApJ, 760, 62
Binney J., Tremaine S., 1987, Galactic Dynamics, Princeton University Press, Princeton, NJ
Blakeslee J. P. et al., 2009, ApJ, 694, 556
Blom C., Spitler L. R., Forbes D. A., 2012, MNRAS, 420, 37
Brockamp M., Küpper A. H. W., Thies I., Baumgardt H., Kroupa P., 2014, MNRAS, 441, 150

Brodie J. P., Romanowsky A. J., Strader J., Forbes D. A., 2011, AJ, 142, 199
Brüns R. C., Kroupa P., 2012, A&A, 547, A65
Calderón J. P., Bassino L. P., Cellone S. A., Richtler T., Caso J. P., Gómez M., 2015, MNRAS, 451, 791
Capuzzo-Dolcetta R., Mastrobuono-Battisti A., 2009, A&A, 507, 183
Caso J. P., Richtler T., Bassino L. P., Salinas R., Lane R. R., Romanowsky A., 2013, A&A, 555, A56
Caso J. P., Bassino L. P., Richtler T., Calderón J. P., Smith Castelli A. V., 2014, MNRAS, 442, 891
Caso J. P., Bassino L. P., Gómez M., 2015, MNRAS, 453, 4421
Caso J. P., Bassino L. P., Gómez M., 2017, MNRAS, 470, 3227
Caso J. P., Bassino L. P., Richtler T., Salinas R., 2019, MNRAS, 483, 4371
Charlton P. J. L., Hudson M. J., Balogh M. L., Khatri S., 2017, MNRAS, 472, 2367
Chiboucas K. et al., 2011, ApJ, 737, 86
Cho J., Sharples R. M., Blakeslee J. P., Zepf S. E., Kundu A., Kim H.-S., Yoon S.-J., 2012, MNRAS, 422, 3591
Choksi N., Gnedin O. Y., Li H., 2018, MNRAS, 480, 2343
Ciotti L., 1991, A&A, 249, 99
Conroy C., Wechsler R. H., Kravtsov A. V., 2006, ApJ, 647, 201
Cora S. A. et al., 2018, MNRAS, 479, 2
Côté P. et al., 2007, ApJ, 671, 1456
Das P., Gerhard O., Mendez R. H., Teodorescu A. M., de Lorenzi F., 2011, MNRAS, 415, 1244
Dirsch B., Richtler T., Geisler D., Forte J. C., Bassino L. P., Gieren W. P., 2003, AJ, 125, 1908
Dirsch B., Schuberth Y., Richtler T., 2005, A&A, 433, 43
Durrell P. R. et al., 2014, ApJ, 794, 103
Escudero C. G., Faifer F. R., Bassino L. P., Calderón J. P., Caso J. P., 2015, MNRAS, 449, 612
Escudero C. G., Faifer F. R., Smith Castelli A. V., Forte J. C., Sesto L. A., González N. M., Scalia M. C., 2018, MNRAS, 474, 4302
Faber S. M., Wegner G., Burstein D., Davies R. L., Dressler A., Lynden-Bell D., Terlevich R. J., 1989, ApJS, 69, 763
Faifer F. R. et al., 2011, MNRAS, 416, 155
Ferrarese L. et al., 2006, ApJS, 164, 334
Forbes D. A., 2017, MNRAS, 472, L104
Forbes D. A., Forte J. C., 2001, MNRAS, 322, 257
Forbes D. A., Remus R.-S., 2018, MNRAS, 479, 4760
Forbes D. A., Grillmair C. J., Williger G. M., Elson R. A. W., Brodie J. P., 1998, MNRAS, 293, 325
Forbes D. A., Sánchez-Blázquez P., Phan A. T. T., Brodie J. P., Strader J., Spitler L., 2006, MNRAS, 366, 1230
Forbes D. A., Spitler L. R., Strader J., Romanowsky A. J., Brodie J. P., Foster C., 2011, MNRAS, 413, 2943
Forbes D. A., Ponman T., O'Sullivan E., 2012, MNRAS, 425, 66
Forbes D. A., Read J. I., Gieles M., Collins M. L. M., 2018, MNRAS, 481, 5592
Forte J. C., Geisler D., Ostrov P. G., Piatti A. E., Gieren W., 2001, AJ, 121, 1992
Foster C. et al., 2011, MNRAS, 415, 3393
Gan J., Kang X., van den Bosch F. C., Hou J., 2010, MNRAS, 408, 2201
Gavazzi G., Boselli A., 1996, Astrophys. Lett. Commun., 35, 1
Geller M. J., Diaferio A., Kurtz M. J., 1999, ApJ, 517, L23
Georgiev I. Y., Puzia T. H., Hilker M., Goudfrooij P., 2009, MNRAS, 392, 879
Glass L. et al., 2011, ApJ, 726, 31
Gómez M., Richtler T., 2004, A&A, 415, 499
Hargis J. R., Rhode K. L., 2012, AJ, 144, 164
Hargis J. R., Rhode K. L., Strader J., Brodie J. P., 2011, ApJ, 738, 113
Harris W. E., 2009a, ApJ, 699, 254
Harris W. E., 2009b, ApJ, 703, 939
Harris W. E., Racine R., 1979, ARA&A, 17, 241
Harris W. E., Harris G. L. H., Barmby P., McLaughlin D. E., Forbes D. A., 2006, AJ, 132, 2187
Harris W. E., Kavelaars J. J., Hanes D. A., Pritchet C. J., Baum W. A., 2009, AJ, 137, 3314
Harris G. L. H., Harris W. E., Geisler D., 2004, AJ, 128, 723
Harris W. E., Harris G. L. H., Alessi M., 2013, ApJ, 772, 82
Hudson M. J., Robison B., 2018, MNRAS, 477, 3869
Hudson M. J., Harris G. L., Harris W. E., 2014, ApJ, 787, L5
Huertas-Company M., Shankar F., Mei S., Bernardi M., Aguerri J. A. L., Meert A., Vikram V., 2013, ApJ, 779, 29
Jordán A. et al., 2004, ApJS, 154, 509
Jordán A. et al., 2005, ApJ, 634, 1002
Jordán A. et al., 2007, ApJS, 171, 101
Jordán A. et al., 2009, ApJS, 180, 54
Jordán A., Peng E. W., Blakeslee J. P., Côté P., Eyheramendy S., Ferrarese L., 2015, ApJS, 221, 13
Kampakoglou M., Benson A. J., 2007, MNRAS, 374, 775
Kapferer W., Sluka C., Schindler S., Ferrari C., Ziegler B., 2009, A&A, 499, 87
Kartha S. S., Forbes D. A., Spitler L. R., Romanowsky A. J., Arnold J. A., Brodie J. P., 2014, MNRAS, 437, 273
Kartha S. S. et al., 2016, MNRAS, 458, 105
King I., 1962, AJ, 67, 471
King I. R., 1966, AJ, 71, 64
Kissler-Patig M., Richtler T., Storm J., della Valle M., 1997, A&A, 327, 503
Klypin A., Yepes G., Gottlöber S., Prada F., Heß S., 2016, MNRAS, 457, 4340
Kochanek C. S. et al., 2001, ApJ, 560, 566
Kravtsov A. V., 2013, ApJ, 764, L31
Kruijssen J. M. D., 2014, Class. Quantum Gravity, 31, 244006
Kruijssen J. M. D., 2015, MNRAS, 454, 1658
Kubo J. M., Stebbins A., Annis J., Dell'Antonio I. P., Lin H., Khiabanian H., Frieman J. A., 2007, ApJ, 671, 1466
Lacerna I., Hernández-Toledo H. M., Avila-Reese V., Abonza-Sane J., del Olmo A., 2016, A&A, 588, A79
Larsen S. S., 1999, A&AS, 139, 393
Li H., Gnedin O. Y., 2014, ApJ, 796, 10
Łokas E. L., Mamon G. A., 2003, MNRAS, 343, 401
Madrid J. P., Leigh N. W. C., Hurley J. R., Giersz M., 2017, MNRAS, 470, 1729
Makarov D., Prugniel P., Terekhova N., Courtois H., Vauglin I., 2014, A&A, 570, A13
Masters K. L. et al., 2010, ApJ, 715, 1419
Moster B. P., Somerville R. S., Maulbetsch C., van den Bosch F. C., Macciò A. V., Naab T., Oser L., 2010, ApJ, 710, 903
Muratov A. L., Gnedin O. Y., 2010, ApJ, 718, 1266
Navarro J. F., Frenk C. S., White S. D. M., 1996, ApJ, 462, 563
Peng E. W. et al., 2006, ApJ, 639, 95
Peng E. W. et al., 2008, ApJ, 681, 197
Perrett K. M., Hanes D. A., Butterworth S. T., Kavelaars J., Geisler D., Harris W. E., 1997, AJ, 113, 895
Planck Collaboration XVI, 2014, A&A, 571, A16
Rhode K. L., Zepf S. E., 2004, AJ, 127, 302
Rhode K. L., Zepf S. E., Kundu A., Larner A. N., 2007, AJ, 134, 1403
Richtler T., 2013, in Pugliese G., de Koter A., Wijburg M., eds, ASP Conf. Ser. Vol. 470, 370 Years of Astronomy in Utrecht. Astron. Soc. Pac., San Francisco, p. 327
Richtler T., Salinas R., Lane R. R., Hilker M., Schirmer M., 2015, A&A, 574, A21
Rodríguez-Puebla A., Behroozi P., Primack J., Klypin A., Lee C., Hellinger D., 2016, MNRAS, 462, 893
Salinas R., Alabi A., Richtler T., Lane R. R., 2015, A&A, 577, A59
Schechter P., 1976, ApJ, 203, 297
Schlafly E. F., Finkbeiner D. P., 2011, ApJ, 737, 103
Schuberth Y., Richtler T., Hilker M., Dirsch B., Bassino L. P., Romanowsky A. J., Infante L., 2010, A&A, 513, A52
Schuberth Y., Richtler T., Hilker M., Salinas R., Dirsch B., Larsen S. S., 2012, A&A, 544, A115
Sersic J. L., 1968, Atlas de galaxias australes, Observatorio Astronómico de Córdoba, Córdoba, Argentina
Sesto L. A., Faifer F. R., Forte J. C., 2016, MNRAS, 461, 4260
Shankar F. et al., 2014, MNRAS, 439, 3189

Shankar F., Bernardi M., 2009, MNRAS, 396, L76
Shen S., Mo H. J., White S. D. M., Blanton M. R., Kauffmann G., Voges W., Brinkmann J., Csabai I., 2003, MNRAS, 343, 978
Sirianni M. et al., 2005, PASP, 117, 1049
Smith R., Sánchez-Janssen R., Fellhauer M., Puzia T. H., Aguerri J. A. L., Farias J. P., 2013, MNRAS, 429, 1066
Spindler A., Wake D., 2017, MNRAS, 468, 333
Spitler L. R., Forbes D. A., 2009, MNRAS, 392, L1
Spitler L. R., Forbes D. A., Strader J., Brodie J. P., Gallagher J. S., 2008, MNRAS, 385, 361
Strader J., Brodie J. P., Forbes D. A., 2004, AJ, 127, 295
Tonini C., 2013, ApJ, 762, 39
Tully R. B. et al., 2013, AJ, 146, 86
Usher C., Forbes D. A., Spitler L. R., Brodie J. P., Romanowsky A. J., Strader J., Woodley K. A., 2013, MNRAS, 436, 1172
Vale A., Ostriker J. P., 2006, MNRAS, 371, 1173
van Dokkum P. G. et al., 2010, ApJ, 709, 1018
Villegas D. et al., 2010, ApJ, 717, 603
Wasserman A. et al., 2018, ApJ, 863, 130
Webb J. J., Leigh N., Sills A., Harris W. E., Hurley J. R., 2014, MNRAS, 442, 1569
Wehner E. M. H., Harris W. E., Whitmore B. C., Rothberg B., Woodley K. A., 2008, ApJ, 681, 1233
Young M. D., Dowell J. L., Rhode K. L., 2012, AJ, 144, 103
Zepf S. E., Ashman K. M., 1993, MNRAS, 264, 611

This paper has been typeset from a TEX/LATEX file prepared by the author.